NTNU

Norwegian University of
Science and Technology

# Investigation of bubble distribution and evolution in solar cell quartz crucibles

Sebastian Holland Hansen

Nanotechnology
Submission date: June 2017
Supervisor: Marisa Di Sabatino, IMA
Co-supervisor: Mari Juel, SINTEF
Astrid Marie Flattum Muggerud, The QUARTZ Corp

Norwegian University of Science and Technology
Department of Materials Science and Engineering

## Acknowledgements

I would like to thank my supervisor Marisa Di Sabatino Lundberg and co-supervisors Mari Juel (SINTEF) and Astrid Marie Flattum Muggerud (The Quartz Corp) for their guidance and feedback throughout the whole master work. I would also like to thank Trygve Lindahl Schanche for helping me with the optical microscopes, Magnus Bentzen Følstad for teaching me how to use the FTIR spectrometer and Ole Tore Buset for training me in using the X-ray tomography scanner. Many thanks to Stein Rørvik for answering my questions regarding X-ray tomography and image analysis. Also, a big thank you to Jonas Einan Gjøvik for helping me with issues related to the VGF furnace and John Atle Bones and Pål Tetlie for supervising the Czochralski puller experiment. Last, but not least, I want to thank Hélène Hendrickx for the good cooperation and for being a valuable discussion partner.

Trondheim, June 2017
Sebastian H. Hansen

# Contents

# List of abbreviations

## Crucible samples

- **STD**: standard (reference) crucible
- **A**: crucible type A
- **B**: crucible type B
- **BC**: bubble containing
- **BF**: bubble free
- **N**: new, unused crucible sample
- **U**: industrially used crucible sample
- **HT**: crucible sample heat treated through experiments in this work
- **C**: coated sample (with barium nitrite)
- **NC**: non-coated sample
- **melt**: sample part immersed in silicon melt
- **top**: sample part outside silicon melt

## Heat treatments

- **HT1**: 1.5 h heat treatment in VGF furnace
- **HT2**: 10 h heat treatment in VGF furnace
- **HT3**: 24 h heat treatment in VGF furnace
- **HTCZ**: 10 h heat treatment in Czochralski puller

## In general

- **VGF**: vertical gradient freeze
- **HE**: heating element
- **ppm**: parts per million

## Abstract

Quartz crucibles are, among other applications, used to produce monocrystalline silicon ingots for the solar cell industry. The crucibles must be of high purity as any gas bubbles or impurities close to the crucible-melt interface may end up in the silicon melt and influence the silicon ingot quality. This master thesis looks at three different fused quartz crucible types, including one reference. The crucibles have been compared with respect to bubble distribution and evolution which then have been related to their quartz sand quality and impurity content. The focus has been on the bubble distribution and evolution in the bubble free (BF) layer. Samples have been taken from the crucible wall and both new and industrially used samples were investigated. Heat treatments in a vertical gradient freeze (VGF) furnace and Czochralski puller have been performed to investigate the secondary bubble growth, the OH content and the micro-bubble formation as a function of heat treatment and crucible type. The results indicate that the sand quality, but also manually controlled processing steps such as crucible fusion, has influence on the bubble growth and BF layer bubble content. A reduction in OH content seems to correlate with increasing bubble growth. The reference (STD) crucible has the largest variation in bubble content and the largest average bubble growth for the samples studied in this work. Crucible B, which has the finest particle size distribution (PSD) and chemistry, seems to be the best choice for silicon ingot production as it experiences, on average, the lowest BF layer bubble growth and has the lowest density of bubbles below detection limit.

# 1 Introduction

Quartz crucibles are essential for the production of silicon for the solar cell industry. Silicon is the most used material for production of solar cells and the silicon ingots, from which solar cell wafers are made, are usually solidified in quartz crucibles. The ingots can be either monocrystalline or multicrystalline. Together, they contribute to about 90 % of the global solar cell market[1]. Monocrystalline solar cells are of higher purity, have less defects and have higher peak efficiencies than multicrystalline cells. The production methods and quality of the crucibles used are important for the final quality. This master thesis focuses on the role of fused quartz crucibles used to make monocrystalline silicon ingots through Czochralski growth. This growth method uses a seed crystal to initialize the crystallization before the silicon ingot is slowly pulled out of the silicon melt during rotation of both crucible and ingot[2]. Quartz crucible properties, related to quartz sand type, structural consistency after fusion and thermal conduction are affected by growth and expansion of nano- and micro-sized bubbles. There is little knowledge on how the bubble growth and expansion are influencing the crucible properties and ultimately the silicon ingot quality. Therefore, there is a need to study this topic as it is relevant both for the photovoltaic and microelectronic industry.

Quartz is the most used crucible material for several reasons. It is available in high purity ores and has a high softening temperature and thermal resistance. Furthermore, it has low thermal expansion and high resistance to thermal shock[3]. These properties make quartz an ideal material for the high temperature process of silicon ingot pulling. A quartz crucible can only be used for production of a few silicon ingots, typically one to three. This is due to a temperature dependent phase transformation that degrades the crucible. At high temperature the polymorph of quartz, cristobalite, forms on the inner and outer surface of the quartz crucible. Cristobalite is brittle and may flake off and into the silicon melt. Although being an inevitable process, the cristobalite can be directed to form a smooth layer by first coating the crucible with a fitting substrate, a so-called devitrification agent. A quartz crucible consists of two layers. The outer layer is known as the bubble containing (BC) layer due to its many macro-sized air bubbles. In this layer the bubbles are essential because of their isolating effect and because they influence the mechanical properties of the crucible by stiffening the quartz structure. This decreases the probability of sag of crucible material. The inner layer is known as the bubble free (BF) layer. In the BF layer bubbles are not wanted. This layer is in direct contact with the silicon melt and typically dissolves by 0.5-2 $mm$ during the silicon ingot pulling. In reality, the BF layer is not completely bubble free as it might contain micro-sized defect bubbles, mainly originating from the air and oxygen in the quartz. The formation of bubbles in the two layers is controlled by removing air from the quartz sand through a controlled vacuum process during crucible fusion. This process is manually controlled. If the vacuuming is not adjusted for properly, bubbles may build up along the the melt border and form lines of bubbles. Another parameter affecting the bubble growth and formation is the OH level of the quartz. A high level of OH groups in the quartz network lowers its viscosity and thus makes it easier for bubbles to expand. Furthermore, at increased temperature the hydrogen may diffuse and form bubbles and thus be a direct source of bubble expansion. Problems occur if the defect bubbles are leaked into the silicon melt during the crystal pulling because they may end up on the crystal solidification front where they may influence the structural development of the silicon ingot. This is why the outermost part of the BF layer is the critical layer to look at when investigating how defect bubbles are influencing the crucible quality.

This master thesis looks at fused quartz crucibles made from three different sand types, including one reference. The crucibles differ with respect to particle size distribution (PSD) and the chemical steps applied during production. The crucibles are further divided into three categories depending on whether they are new, heat treated on an industrial level or heat treated through experiments in this work. Thermal heat treatments in a vertical gradient freeze (VGF) furnace together with X-ray tomography and transmission and reflectance optical microscopy have been used to study the secondary bubble growth and distribution as a function of heat treatment, crucible type and position in the crucible. The main focus has been the bubble growth and distribution in the BF layer. It has also been investigated whether the crucible coating, and thus the degree of cristobalite formation, has an effect on the bubble evolution. A hypothesis that will be tested is whether the cristobalite layer acts as a heat shield, reducing the heat conduction from melt to crucible and thus the bubble expansion in the outermost part of the BF layer. Furthermore, the OH level of the different crucibles has been measured by Fourier transform infrared (FTIR) spectroscopy. As the viscosity of the crucible depends on the OH level and because hydrogen may form bubbles, it will be investigated if the OH level can be correlated to the bubble evolution. A hypothesis to be tested is whether a higher BF layer bubble content can be connected to a reduction in OH content due to diffusion and bubble formation. My previous project work indicates that heat treated crucibles have a higher number of bubbles and the mechanisms behind this will be investigated in this work[4]. A hypothesis is that the extra bubbles can be explained due to the growth of bubbles initially smaller than 10 $\mu m$ in diameter. These bubbles are not detected through the X-ray tomography scans. Transmission light microscopy will be applied to test this.

Finally, all the variables regarding bubble growth and expansion will be connected in order to draw a conclusion on which crucible, among those investigated, is the most promising for monocrystalline silicon ingot production. The work is part of a larger national project (FME-Centre for environmentally friendly energy research) where NTNU, SINTEF, Norsun and The Quartz Corp are among the partners. Furthermore, this work builds on the investigations performed in my Project work[4]. The structure and content of the theory section will therefore resemble that of my Project work.

# 2 Theory

## 2.1 Classification of $SiO_2$ minerals

Silica ($SiO_2$) in crystalline and amorphous form makes up 12.6 weight% of the Earth's crust[6] and thus is one of the most abundant minerals. However, the quartz used for solar cell crucibles is only one of more than 15 silica mineral phases, all with different crystal structure. An overview of the different phases can be seen in Table 1. However, although the crystal structure being different, the basic structure of silica is a network of $SiO_4$ tetrahedra. The more scientific term of ordinary quartz is $\alpha$-quartz or low quartz. The term "low" refers to this being a stable silica polymorph at low temperatures. In this work only "quartz" will be used to refer to the material. Quartz is the only stable silica polymorph at normal ambient conditions and other silica polymorphs will, given enough time, transform into quartz. If being heated at ambient conditions, quartz will undergo a phase transformation into $\beta$-quartz at 573 °C. $\beta$-quartz, which is also known as high quartz, is a high temperature polymorph of silica, but with a crystal structure very similar to that of quartz[5]. The temperature phase transformations of quartz will be looked upon in closer detail in Section 2.7 about cristobalite formation.

Table 1: The $SiO_2$ system[6].

| | | |
|---|---|---|
| **Quartz-tridymite-cristobalite group** | | |
| (atmospheric and low pressure) | Low ($\alpha$)-quartz | Trigonal |
| | High ($\beta$)-quartz | Hexagonal |
| | Tridymite | Monoclinic |
| | High-tridymite | Hexagonal |
| | Cristobalite | Tetragonal |
| | High-cristobalite | Cubic |
| | Melanophlogite | Cubic |
| | Fibrous $SiO_2$ | Orhtorhombic |
| | Moganite | Monoclinic |
| **Keatite-coesite-stishovite group** | | |
| (high and ultra pressure) | Keatite | Tetragonal |
| | Coesite | Monoclinic |
| | Stishovite | Tetragonal |
| | Seifertite | Orthorhombic |
| **Lechatelierite-opal group** | | |
| (amorphous phases) | Lechatelierite | Natural silica glass |
| | Opal | $H_2O$-bearing, solid $SiO_2$ gel |

$\alpha$-quartz is used for many industrial and technical purposes, such as crucible production. However, geological variations result in different mineral variations with respect to e.g. trace elements and isotope composition. Furthermore, specific point defects and dislocations may have been incorporated in the quartz during crystallization. This causes variations, also within the same mineral phases[6]. Therefore, the quartz deposition site has to be carefully selected in the search for quartz with the ideal composition and purity. There are few deposits in the world that fulfil the strict requirements as crucible material. The quartz studied in this master thesis has its origin in the

Spruce Pine deposit in North Carolina.

## 2.2 Quartz sand processing

Even small traces of impurities and defect bubbles in the BF layer of a fused quartz crucible may have serious impact if leaked into the silicon melt. Therefore, the quality demand for the quartz sand used is high. The degree of impurities in the processed quartz sand is reduced to less than 25 parts per million (ppm) before it can be used as crucible material. The main minerals found in the quartz ore taken from the Spruce Pine deposit are feldspar, garnet and mica. There will also be smaller traces of elements like iron, alumina, titanium, calcium and sodium[7]. These minerals and elements are removed from the quartz sand by using so-called comminution technology. Comminution implies reducing the raw quartz to the required size and removing the unwanted impurities. The process include the following main steps[6]:

- Pre-processing
- Physical processing
- Chemical leaching
- Thermal treatment

The main purpose of the pre-processing step is to reduce the size of the mined quartz. This is accomplished through crushing and grinding and makes it easier to handle the quartz and to separate out impurities. The smaller the grains are, the larger their surface to volume ratio is. Thus, more impurities will be exposed at the quartz grain surface which makes it easier to remove them. Crushing involves reducing the ore down to particles in the size range of 1-10 $cm$. The two main principles used for crushing are compression and impact. Grinding reduces the quartz pieces to sizes below 500 $\mu m$ and is typically done in a ball or rod mill. As can be seen in Figure 1, these mills consist of a hollow cylinder rotating about its axis. The cylinder contains either balls or rods made of e.g. stainless steel that works as the grinding media to reduce the size of the silica grains on impact[8]. The crushing and grinding may introduce contamination due to wear of the equipment. Therefore, alternative techniques like electrodynamic fragmentation are sometimes used. Electrodynamic fragmentation uses a high voltage discharge to generate shock waves within the quartz causing it to break along the grain boundaries[6]. This method is ideal for selective removal of gas and liquid inclusions.

The impurities that were exposed during the pre-processing step are removed through physical processing. First, attrition is done to clean the quartz particles. Then the quartz sand goes through magnetic separation to remove magnetic minerals that were not washed away during attrition. This implies the use of electromagnets to sort out paramagnetic or ferromagnetic impurities such as iron. Quartz is diamagnetic and thus repelled. The magnetic separation happens through several steps and at different field strength. The quartz sand is in slurry form at this stage. Thus, by letting the slurry pass through a magnetic grid, the magnetic minerals are attracted by the field.

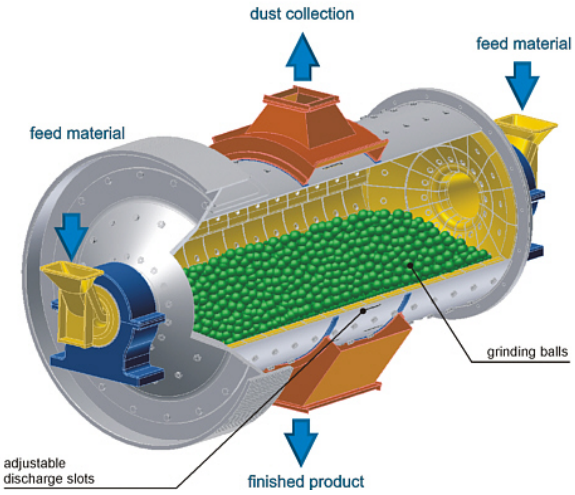


Figure 1: Schematic view of a ball milll[11].

Flotation is a separation process that separates minerals with respect to their ability to be wetted[6]. Minerals like feldspar, garnet and mica are separated out. More precisely, flotation utilizes the fact that minerals have different zeta potentials at different pH and thus different electrovalent adsorption affinity. In practice, hydrophilic and hydrophobic components are separated by mixing the quartz sand with water in a large container called a flotation cell. Surfactants called collector chemicals are added to the slurry. These adsorb on the surface of the minerals that are to be separated out to increase their hydrophobicity. As seen in Figure 2, an inlet of air is introduced at the bottom of the flotation cell to create a stream of bubbles moving towards the surface. So-called frothing agents are introduced that bind to the surface of the air bubbles. The hydrophobic minerals then bind to the air bubbles and form a froth layer on the water surface that can later be removed. The wanted minerals stay in the water phase, which in this case is the pure quartz sand. The process may be repeated several times[8][9][10].

Chemical treatment is applied after physical processing to remove surface impurities. Chemical treatment typically includes acid washing and leaching. Leaching is a form of acid washing, but which uses the strong acid hydrofluoric acid (HF) at elevated temperature[6]. This is a more effective impurity removal method than acid washing with less aggressive acids. Feldspar has higher etch-rate than pure quartz. Still, it is important to ensure that the leaching is not run for too long and disintegrates the quartz as well[8]. After leaching, the quartz sand is thoroughly cleaned with water.

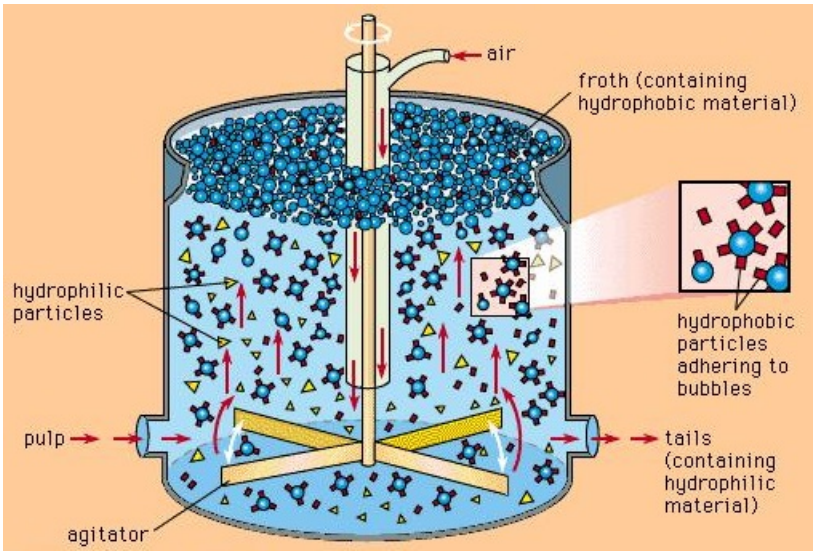


Figure 2: Schematic view of a flotation cell[12].

The last processing step is the thermal treatment where the quartz sand is de-watered and dried. The removal of fluid inclusions improves the melting behaviour of the quartz sand and is a critical step to reduce the bubble formation. For the top grade sand types chlorination may also be applied. Chlorination implies heating the quartz in a chlorine atmosphere to reduce the level of alkali metal impurities. A last dry magnetic separation step may be applied to remove any last traces of magnetic minerals. Furthermore, the quartz sand usually goes through a high temperature calcining treatment (above 800 °C) to burn off any organic residues before it is ready for use as crucible material. The heat treatment is, however, primarily done to change the quartz color to white[6].

## 2.3 Production of fused quartz crucibles

Quartz crucibles used for production of monocrystalline silicon ingots are commonly referred to as fused quartz crucibles. Fused quartz is glass which only contains silica ($SiO_2$). It thus differs from more common variants of glass in that it does not contain any additives. This results in fused quartz having a high melting temperature[13]. There are different ways of making fused quartz crucibles and the methods vary from company to company. However, the main steps are rather general. High purity crystalline quartz sand is poured into a hollow mold rotating about its vertical axis. The most used mold material is graphite. Graphite is used due to its relatively low price, its availability as large blocks and its ability to withstand high temperature. Furthermore, graphite has good thermal properties, a high sublimation point and is a quite good conductor of heat and electricity, which also makes it suitable as heater material[14]. Depending on the crucible type and the wanted properties, the same quartz sand can be used for the whole crucible, or alternatively, different sand types can be used for the outer (BC) and inner (BF) layer. The rotation of the mold creates a centrifugal force that presses the quartz sand against the wall. Heat is then supplied from an electric arc. The melting takes place at around 1650 °C. The crucible sand is heated and melts

from the inside and outwards. Vacuum is necessary to suck out air from the pores in the melting quartz sand. This is especially important for the inner layer as this is not supposed to contain any air bubbles. The vacuum is adjusted for manually. If there is any delay in the movement of the melt border, bubbles may start to form along the border in lines if the vacuum is not adjusted for properly. The bubble lines are more often seen in crucibles of low quartz sand quality[15]. An example on formation of such a line of bubbles can be seen in Figure 3. At last the finished crucible is ejected from the housing by introducing compressed air[4][16][17].

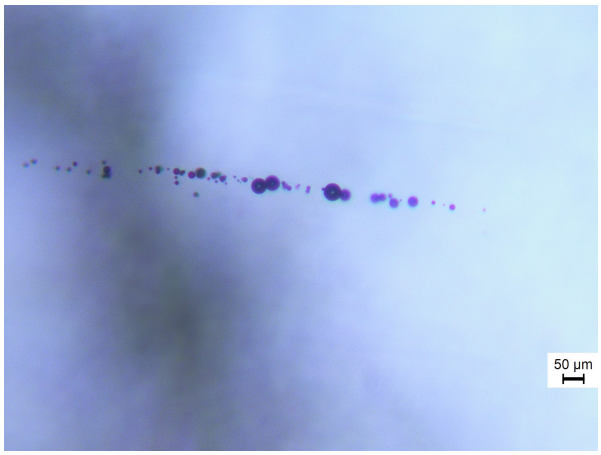


Figure 3: Transmission light microscopy picture of a line of bubbles having formed at the moving melt border during crucible fusion.

## 2.4 The Czochralski process

The Czochralski process is one of the most used methods for single crystal growth. The silicon crystal is grown from a silicon melt by starting with a crystal seed mounted on a rod. When the seed is dipped into the melt it initializes the crystallization process. Then, as seen in Figure 4, the seed is gradually pulled out of the melt in a rotary manner. The melt solidifies on the surface of the seed to give a long cylindrical crystal with the same crystal orientation as the original seed. Heat is applied by a hot-zone made of a twisted graphite electrode surrounding the crucible. To ensure that the silicon melts properly, the temperature prior to seed contact is close to 1500 °C in the center part of the melt. The inner layer of the quartz crucible may dissolve into the melt with about 0.5-2 $mm$ during the crystal pulling. It is therefore important that the inner crucible layer is free of bubbles, defects and impurities. Bubbles at the melt border that rupture may introduce quartz particulates into the silicon melt. Quartz particulates may end up in the silicon crystal and cause pinhole defects or interrupt the single crystal growth, e.g. by providing a site for cooled silicon to solidify and form a secondary crystal from the quartz crucible[16]. There may be several hours of difference between how long it takes to pull one crystal. Thus, the amount of quartz crucible that dissolves into the melt varies. A typical crystal pulling, however, lasts around 100 hours from the silicon is melted until the crystal is finished.

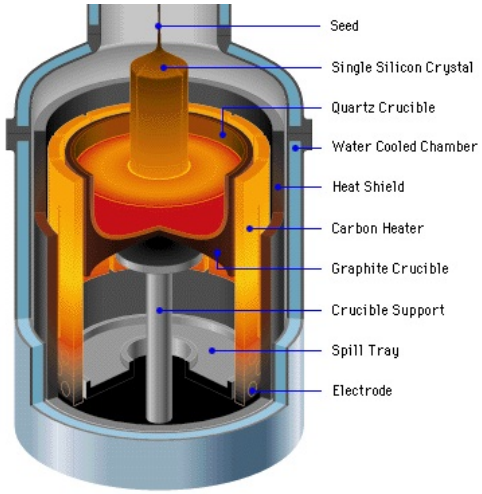


Figure 4: Schematic view of the Czochralski crystal pulling process[18].

When the crystal seed is lowered into the silicon melt, it experiences a thermal shock due to the temperature differences. This results in dislocations in the silicon crystal. A solution to the problem is to pull the first part of the crystal at a high pulling rate. The silicon crystal thus gets a thin neck at the top. If the crystal is grown fast and thin enough, the dislocations tend to grow out from the sides of the neck and are thus excluded from the main body of the crystal. The dislocations usually have the $< 110 >$ vector as the preferred axis. Thus, by growing the rod in the $< 100 >$ or $< 111 >$ direction one can by a simple mean reduce the number of dislocations[4][14]. It is also important to ensure a stable temperature and rotation of seed and crucible. When the formation of the neck is completed, the pulling rate and/or the temperature is decreased to increase the diameter of the crystal. The crystal main body is then grown by keeping the pulling rate at a constant pace and the temperature at a constant level. Adjustments have to be done as the crystal is gaining mass to compensate for the decreasing melt level. When the desired length of the main body is reached, the pull rate is increased once more to reduce the crystal diameter. This results in a end-cone or tail and is done for the same reasons as the neck formation[4][19].

## 2.5 Bubbles in the crucible

### 2.5.1 Crucible layers

The crucible is divided into two layers with respect to bubble content. During crystal pulling the inner or bubble free (BF) layer is in contact with the silicon melt. The outer or bubble containing (BC) layer is covering the inner layer. This is shown in the cross-section of a quartz crucible in Figure 5. The bubbles in the BC layer contain air which have lower heat capacity than the surrounding quartz. Thus, the bubbles contribute to the good insulating properties of the crucible[22]. Furthermore, the bubbles in the BC layer influence the mechanical properties of the crucible by stiffening the quartz structure. This decreases the probability of sag of crucible material.

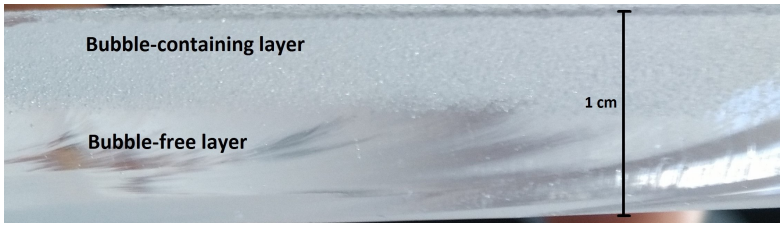


Figure 5: Cross-section of a fused quartz crucible showing the BC and BF layer. The BF layer is not completely translucent because the cross-section has not been polished.

The inner layer of the crucible dissolves by 0.5-2 $mm$ during the crystal pulling depending on the holding time and quartz sand quality. To prevent impurities from entering the silicon melt it is therefore important to keep the dissolving part of the inner layer free of bubbles. It has been shown that the bubbles do almost not move spatially, even at temperatures around 1500 °C [23]. Thus, only the defect bubbles at the crucible-melt interface may cause ruptures and allow for gas and impurities to enter the silicon melt. The main contributor to the bubble gas is air, of which the main components are nitrogen and oxygen gas. Furthermore, quartz ($SiO_2$) consists of oxygen and silicon. Some of this oxygen forms oxygen gas which contributes to the formation of SiO gas through partial reduction of silica with silicon. Any gas bubbles that leak into the melt follow the circulation caused by the crucible rotation and may eventually adsorb on the ingot surface or solidification front where they create gas pockets leading to structural losses. These gas pockets are commonly reffered to as pinhole defects and typically have a diameter in the range of 50 $\mu m$ - 2 $mm$[21].

### 2.5.2 Bubble growth and expansion

As seen in Figure 6, the bubble volume increases significantly during Czochralski crystal pulling. The internal pressure of the bubbles in the crucible is higher than that of the vacuum in the furnace. Thus, the bubbles expand when the viscosity of the quartz becomes low enough due to the increasing temperature[16]. As seen in my project work "Characterization of quartz crucibles for silicon solar cell production"[4], the average volume expansion ratio from the new to used crucibles under investigation was 305. Thus, the used crucibles has, on average, a bubble volume 305 times larger than that of the new crucibles. To be able to control the bubble growth in the BF layer it is important to understand the bubble formation mechanisms. It can be distinguished between the growth of already existing bubbles, so called primary bubble growth, and the formation and growth of new bubbles due to impurities in the quartz, so called secondary bubble growth. The degree of primary bubbles depend to a large degree on the control of the fusion process during crucible manufacturing. The degree of secondary bubbles, however, is dependent on the impurity content in the quartz. Carbon is such an impurity. Carbon can be introduced to the quartz through the graphite mold used for producing the crucible, through the graphite electrodes used as heating elements and graphite support and isolation parts used during the Czochralski pulling. Carbon may react with the quartz, creating CO and SiO gas, through the following reactions[24]:

$$SiO_2(s) + C(s) \rightarrow SiO(g) + CO(g) \tag{1}$$

$$SiO(g) + 2C(s) \rightarrow SiC(s) + CO(g) \tag{2}$$

According to Huang et al.[21], carbon is the source of bubbles undergoing huge expansion. These are bubbles that obtain a diameter of typically more than 500 $\mu m$. These bubbles are rarely found in high quality quartz crucibles. However, if present, they may cause large ruptures at the melt border.

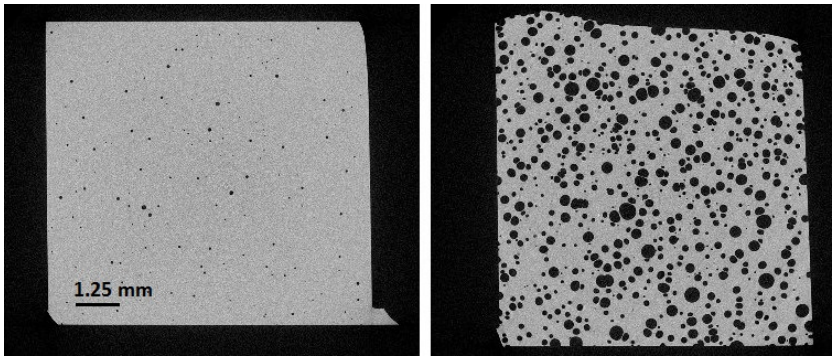


Figure 6: Tomographic cross-sections of the BC layer of a new (left) and used (right) quartz crucible of the same sand type.

### 2.5.3 Formation of bubbles at the crucible-melt interface

Cavities in the quartz crucible will release their gas content when being exposed to the silicon melt. The cavities may also be the origin of continuous bubble formation at contact with the melt. Inside the furnace chamber during crystal pulling there is an argon atmosphere. Experiments have shown that in the presence of argon, bubbles form in the quartz cavities immediately after the cavities come into contact with the melt[21]. Equivalent experiments were performed in near vacuum with almost no argon flow, and then no bubbles were formed. This indicates that bubbles formed in the cavities at the crucible-melt interface to a large degree are filled with argon.

### 2.5.4 The effect of OH groups

OH groups are incorporated into the quartz network, as illustrated in Figure 7, through reaction with water. The reaction is described by the following equation[35]:

$$Si_2O + H_2O \rightarrow 2SiOH \tag{3}$$

Water forms during crucible manufacturing when hydrogen gas reacts with oxygen. Hydrogen gas is introduced during crucible fusion to combine with oxygen and thus prevent the oxygen from damaging the heat elements. The crucible is then heat treated to make the water and OH-groups diffuse out of the quartz structure. The OH content is the major chemical parameter affecting the viscosity of the crucible. The higher the OH content, the lower the viscosity of the quartz is. A lower viscosity causes the crucible to sag more at high temperature. Furthermore, bubbles may more easily expand when the quartz softens.

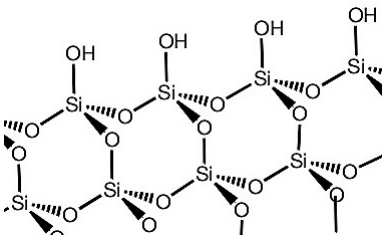


Figure 7: Schematic view of how OH groups are incorporated into the quartz structure[25].

## 2.6 Temperature distribution in the crucible

In order to better understand the formation and growth of bubbles inside the crucible, it is necessary to know how the temperature is distributed through the crucible during crystal pulling. As seen in Figure 4, heat is supplied to the silicon melt by heat elements positioned outside the crucible. F. W. Thorsen used a CGSim simulation to obtain temperature distribution graphs for the crucible during crystal pulling in his master thesis[26]. Some of the results are summarized in Figure 8.

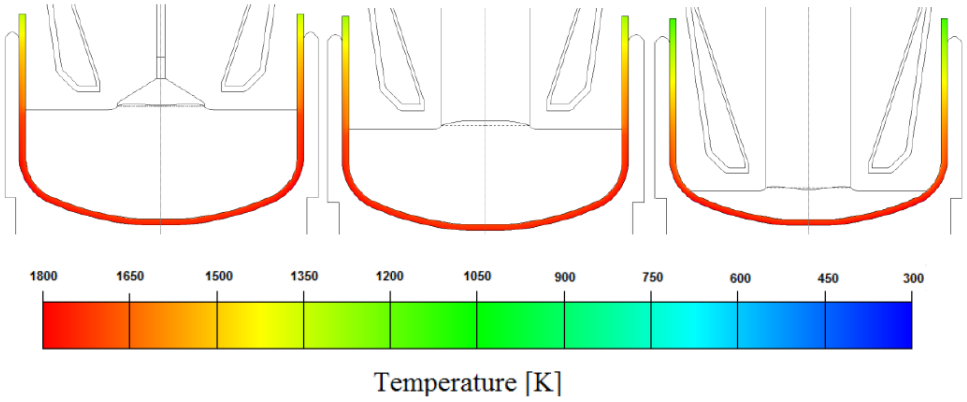


Figure 8: Temperature distribution in the crucible at the beginning (left), during (middle) and after (right) crystal pulling[26].

Thorsen's results show that the bottom of the crucible experiences higher temperatures than the top. It can be seen from Figure 8 that the temperature at the top of the crucible is reduced with decreasing melt level. Furthermore, the lower part of the crucible that is in contact with the melt has a temperature which is more stable. Thus, it could be expected that the lower parts of the crucible would be subject to a higher degree of bubble growth. However, as will be discussed later in this work, the opposite situation seem to be the case. Results from the same dataset show that the temperature in general is higher in the outer layer of the crucible. This is to be expected due to the positions of the heating elements.

## 2.7 Cristobalite formation

Quartz experiences phase transformations with changes in temperature which alters its density and crystal structure. This has implications for the quartz crucible during crystal pulling. As illustrated in Figure 9, trigonal $\alpha$-quartz forms into hexagonal $\beta$-quartz at 573 °C[5]. At 1470 °C another phase transformation occurs when $\beta$-quartz transforms into cubic $\beta$-cristobalite. If heated further, the cristobalite eventually starts to melt at a temperature around 1700 °C.

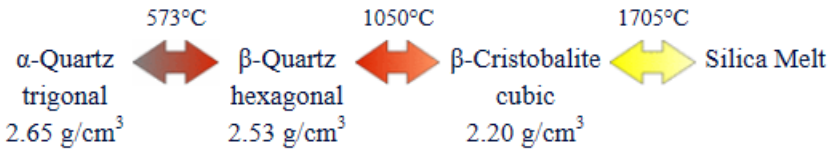


Figure 9: Illustration of the phase transformations of quartz during controlled heating[5].

It is the cristobalite that is a concern during crystal pulling. The pulling is performed at temperatures around 1500 °C which is above the phase transformation temperature of cristobalite. This means that cristobalite will start to form on the inner layer of the quartz crucible. For comparison, Figure 10 shows a piece of a used quartz crucible with cristobalite layer and a piece of unused quartz crucible without. Because the melting point of cristobalite is higher than 1700 °C, it withstands the operating conditions of the Czochralski process[20]. The reason why the whole quartz crucible does not transform into cristobalite is because the outer cristobalite layer acts as a heat shield between the crucible and melt and thus slows down the process of phase transformation. However, it is unclear to what degree this is of importance for the bubble formation and expansion in the outermost part of the BF layer. It should be considered that if quartz is heated quickly, the $\beta$-quartz phase skip the cristobalite transition. This implies that the quartz melts at a lower temperature[5].

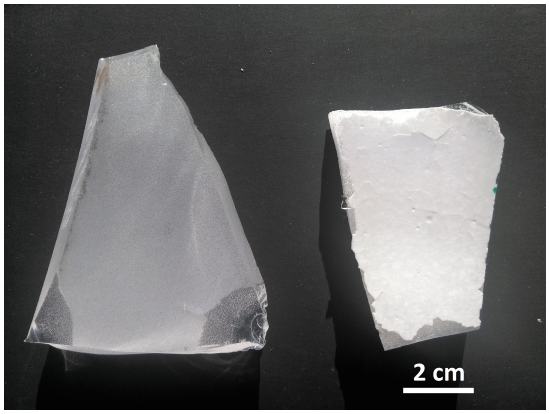


Figure 10: Picture showing a fragment of a used quartz crucible with a white cristobalite layer to the right and a fragment of an unused crucible without cristobalite layer to the left.

The formation of cristobalite is inevitable. Although it may act as a heat shield, this is a process that decreases the density and degrades the quality of the inner crucible surface. The porous cristobalite

layer increases the risk of leakage of bubbles and impurities into the silicon melt. Furthermore, contaminants on the inner surface of the crucible may act as nucleation centres for cristobalite islands. These islands can be released as particles into the silicon melt and eventually cause dislocations in the silicon ingot. Another point of concern is the phase transformation from the beta to alpha phase upon cooling of the crucible. The phase transformations illustrated in Figure 9 are reversible as long as the temperature changes slowly. However, in practice not all cristobalite will transform back to quartz and this is why a quartz crucible only can be heat treated once. When cristobalite transforms back into the $\alpha$-quartz there will be a volume contraction. More precisely, cristobalite experiences a 0.8 volume % change for a 30 °C volume window during the phase transformation[20]. This is a source of crack formation. It is not possible to prevent the phase transformation. However, the growth of cristobalite can be controlled. This is accomplished by using so-called devitrification agents, such as barium nitrite. These can be spray- or dip-coated onto the crucible to promote the cristobalite formation and typically include oxides, hydroxides, carbonates or silicates of an alkaline earth metal. The promoter provides nucleation sites on the surface of the crucible, enabling the quartz to crystallize and form a complete shell of beta-cristobalite. A complete cristobalite layer is less likely to flake off into the silicon melt[4].

## 2.8 Economical aspects of quartz crucible production

The production of fused quartz crucibles for monocrystalline silicon ingot production is a balance of quality versus price. The quality of the crucibles should be high to ensure production of silicon ingots with low impurity content when at the same time the production cost per crucible has to be pressed down to be able to compete on a global market. The question that the crucible manufacturers have to ask themselves is: "what is the cheapest crucible that can be produced that gives sufficient quality?" It is the processing of the quartz sand that to a large degree determines the price of the crucible. Extra chemical steps, like e.g. chlorination, may be applied to reduce the content of alkali impurities. This increases the total cost. However, quartz sand of higher purity is not necessarily equivalent to a better performing crucible. This is because, as discussed in Section 2.3, the fusion of the crucible influences the bubble formation. Thus, a crucible with quartz sand of the highest purity may still have a high content of BF layer bubbles if the vacuum process during crucible fusion has not been controlled properly. The performance of quartz crucibles may typically be measured in yield and productivity. The yield is how much of the silicon ingot produced in the crucible that has quality high enough to be used for silicon wafer production. The crown and tail has to be cut off before the ingot can be sliced into wafers. The more impurities in the silicon melt, the more dislocations there will be in the silicon ingot and thus the crown will have to be grown longer before the ingot body can be grown dislocation free. The same applies for the tail. This reduces the yield. The productivity is usually measured in kg ingot produced per week[15].

## 2.9 Characterization tools

### 2.9.1 X-ray tomography

Tomography refers to imaging of sections of an object through the use of a penetrating wave. X-ray tomography is a non-destructive technique that enables visualization of the 3D interior structure of real objects with high spatial resolution. This makes it possible to do detailed microstructural analysis of many different kinds of materials with little or no sample preparation. As seen in Figure 11, a typical X-ray tomography set-up includes an X-ray source, X-ray detector and a rotational

sample stage. An electron beam is generated by heating a tungsten filament. The electron beam is then directed onto the atoms in the target element which causes the electrons of the atoms to be ejected from the inner shells. When a hole in the inner shell is filled by an outer shell electron, a characteristic X-ray photon is emitted. The image is obtained by detecting either the attenuation or the phase shift of the X-ray beam transmitted through the sample. The stronger the X-ray attenuation, the darker the corresponding part in the projected image will be. The attenuation is given by the Beer-Lambert law which describes the intensity reduction as a function of X-ray energy, X-ray path length and the absorption coefficient:

$$I(x) = I_0 e^{-\alpha x} \tag{4}$$

where $I_0$ and I are the initial and final X-ray intensities respectively, $\alpha$ is the material's linear absorption coefficient and $x$ is the length of the X-ray path[2].

Images for many different angular positions are taken. This results in a set of projections that can be used to reconstruct 2D layers or slices through the object. By stacking these slices together, it is possible to visualize the structure in 3D. The most common method for converting the X-ray attenuation data into an image is called "filtered back-projection". The linear attenuation data collected from each angle are then convolved with a specially designed filter and projected back across a pixel field at the same angle. A limitation of X-ray tomography is that the resolution is limited to about 1000-2000x the object cross-section diameter. Thus, high resolution requires small samples. Furthermore, not all features have large enough attenuation contrast to be useful for imaging[4][27][28][29].

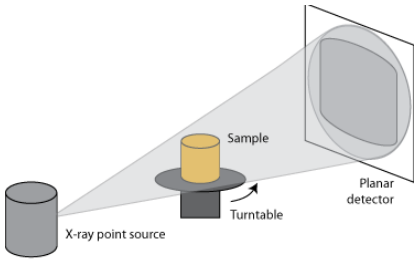


Figure 11: Schematic view of the basic set-up of an X-ray tomography scanner[28].

### 2.9.2 Optical microscopy

The optical microscope represents the simplest form of microscopy. Nevertheless, it is a useful technique that is often applied as a first method to study a sample. The optical microscope uses visible light and a set of lenses to magnify the image of the sample. As seen in the schematic set-up in Figure 12, a typical compound transmission microscope has a condenser lens that concentrate the light from the illumination source. The lens close to the sample, called the objective lens, then focuses the light to a real image of the sample that is magnified by a group of lenses called the eyepiece. The image seen through the binoculars is a virtually enlarged image of the sample. A disadvantage of the optical microscope is its diffraction limit. This implies that its resolution is

limited due to diffraction of light. It occurs when the apertures are on a similar lengthscale to the wavelenght, which typically is at a few hundred nanometers. The main advantages of optical microscopy are that it is quick, easy and simple to use[4][30].

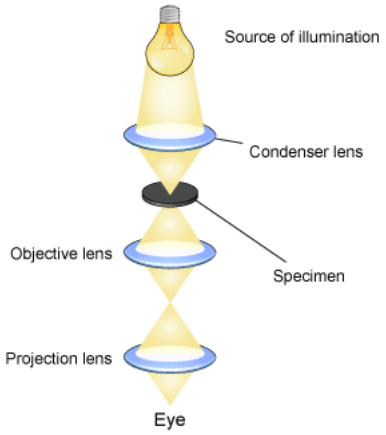


Figure 12: Schematic view of an optical compound transmission light microscope[32].

### 2.9.3 FTIR spectroscopy

Infrared (IR) spectroscopy is an analysis technique that obtains the IR spectrum of a liquid, solid or gas. When a beam of light is shone through a sample, the different molecules in the sample absorb light at specific wavelengths depending on their vibrational energy levels. Upon absorption, the dipole moment of the sample molecules change as the vibrational energy level is transferred from ground to excited state[34]. The recorded loss in intensity at specific wavelengths results in a spectrum with absorption peaks indicating different molecular groups, where the frequency of the absorption peak is determined by the vibrational energy gap. Fourier transform spectroscopy differs from the more basic dispersive spectroscopy in that instead of using a monochromatic light source, a polychromatic beam containing many different wavelengths is used. The total intensity of the beam is measured before it is modified to contain another combination of wavelengths which gives a second data point. This process is repeated several times and a computer uses the Fourier transform as an algorithm to calculate how much light is absorbed at each wavelength. The advantage of using a polychromatic light source is that the intensity can be measured over a wide spectral range.

A typical FTIR spectrometer consists of a light source, interferometer, sample compartment, detector, amplifier, A/D convertor and computer. The generated polychromatic IR beam passes into a configuration of mirrors known as a Michelson interferometer. One mirror is stationary while another is movable. A beam splitter is used to transmit 50 % of the light towards the fixed mirror and reflect 50 % towards the moving mirror. The beams are then reflected and recombined at the beam splitter. The difference in the path length of the beams is known as the retardation. A part of the beam then passes into the sample compartment and then the detector. Because the movable

mirror moves back and forth, the intensity of the signal increases and decreases which gives rise to a cosine wave. The resulting plot is called an interferogram and is obtained by recording the beam signal for different values of the retardation. The Fourier transform is then applied to the interferogram to obtain the spectrum. Advantages of Fourier transform spectroscopy compared to dispersive spectroscopy are that the signal-to-noise ratio is higher for a given scan time, the resolution is extremely high, the scan range is wider and the scan time is often shorter[33][34].

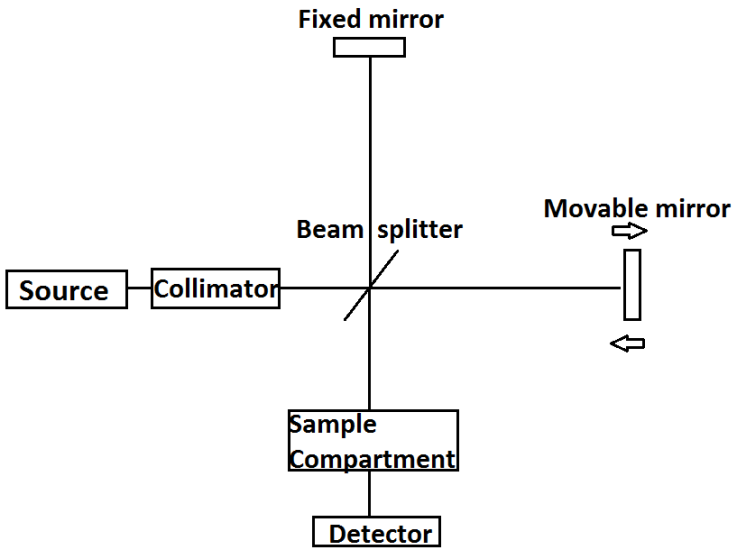


Figure 13: Schematic view of an FTIR set-up.

# 3 Experimental

## 3.1 Crucible types and abbreviations

Three different crucible types, including one reference, were investigated. As the real names of the crucibles can be linked to confidential information about their sand quality and production, they are in this report referred to as STD, A, and B. STD is an abbreviation for "standard" which is the reference crucible. The letters N, U and HT used in later sections refer to whether the crucible is new (N), used (U) or heat treated (HT) during the experiments in this work. HT1, HT2, HT3 and HTCZ refers to the 1.5 hour, 10 hour, 24 hour and Czochralski heat treatment, respectively. The letters C and NC refers to whether the crucible is coated (C) or non-coated (NC). The following table gives a general overview of the differences in sand quality and chemistry between the crucibles.

Table 2: Differences in crucible sand quality and chemistry.

| Crucible | Sand quality | Chemistry |
|---|---|---|
| STD | Coarse | Standard |
| A | Coarse | Standard |
| B | Fine | Standard+ |

A "fine" sand quality refers to a finer particle size distribution (PSD) of the quartz sand grains. A "Standard+" chemistry refers to the finer chemistry that the B sand obtains as a result of its finer PSD (See explanation in Section 2.2 regarding quartz sand processing).

## 3.2 Sample material

Each crucible type came in both new and used pieces, where for each of these there was a piece that was coated with barium nitrite and one that was not. The exception was crucible STD which only came in the coated version. Samples were cut for the X-ray tomography scanning from both the new and used pieces. Two cubes with dimensions 1x1x1 $cm$ were cut for each crucible type. This resulted in two sample series that will later be reffered to as Series 1 and 2. As can be seen in Figure 14, the cubic wall samples were cut 12 $cm$ below the top of the crucible and from positions right next to each other. Furthermore, from the same crucibles, 2 $mm$ thick samples were cut for FTIR spectroscopy from same position as the cubes. The rod samples for the heat treatment experiments were also cut from a position with their top at a position 12 $cm$ below the top of the crucible. The rods had a length of about 5 $cm$ and were cut out vertically. However, the rods used in the Czochralski puller experiment were cut from a position 17 $cm$ below the crucible top due to lack of material. These rods had a length of 10 $cm$.

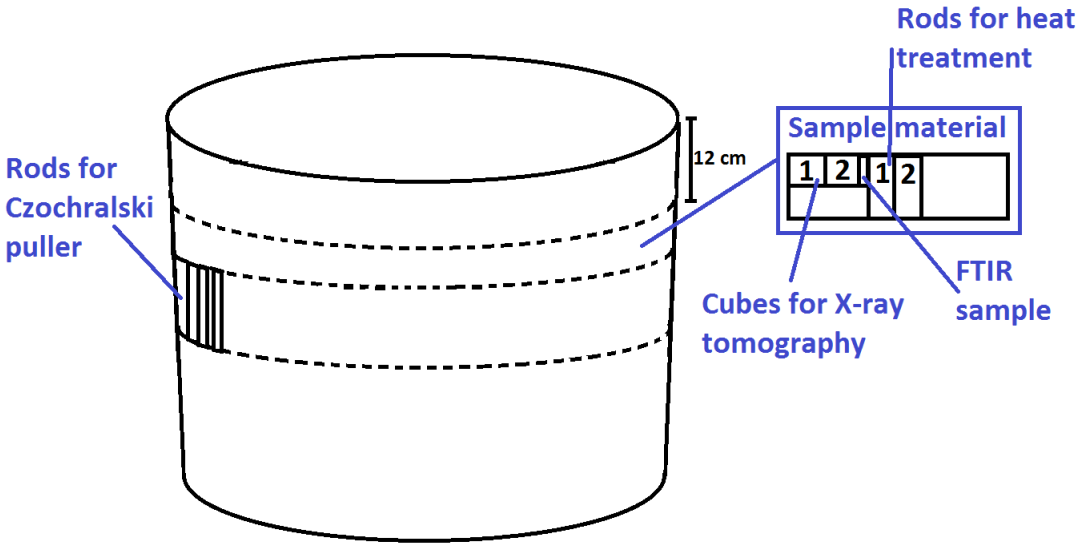


Figure 14: Schematic view of a crucible showing the areas from which the samples were cut.

## 3.3 Sample preparation

### 3.3.1 X-ray tomography samples

The preparation of the samples for X-ray tomography was done by first manually cutting the quartz crucible pieces with a coarse circular diamond blade saw, as seen in Figure 15a, to reduce their size. Then, as seen in Figure 15b, a diamond blade Accutom high precision saw was used to fine cut these pieces into cubes of 1 $cm^3$ using a cutting speed of 0.070 $mm/s$. For some of the more porous cristobalite samples the cutting speed was reduced to 0.060 $mm/s$. The quartz rods used in the heat treat experiments were cut with the coarse diamond blade saw only.

(a) (b)

Figure 15: Pictures of the coarse diamond blade saw (a) and the Accutom high precision saw (b).

For the Accutom high precision saw the cutting itself proceeded automatically. The sample was fastened to the sample holder and the wanted cutting speed was typed in. However, a straight cut relied on how the sample was fastened to the holder. The saw does not have any angle measurement system and every measurement must be done visually. It proved to be a problem that the thin quartz rods tended to slip in the sample holder and thus cause an uneven cut. One solution was to fasten the samples tighter in the sample holder. However, this increased the risk of sample cracking or a broken cristobalite layer due to the high mechanical stress. The best solution proved to be to fasten a wider piece of quartz in the sample holder and cut the cubes from this. This provided more stability during the cutting and made it easier to cut straight. Another aspect that made cutting straight difficult was the curvature of the crucible pieces. As nothing could be done with the curvature, the only precaution that could be made was to only fasten short crucible segments in the sample holder. This reduced the effect of the curvature and made it easier to cut cubes with straight corners. During polishing the biggest concern was that small particles would break off and scratch the polished surface. The probability of this was minimized by washing both the samples, sample holder and polishing cloth before a new run.

### 3.3.2 FTIR samples

The samples for the FTIR spectroscopy analysis were cut out from the crucibles in the same way as for the cubic crucible samples. The only difference was the sample thickness, which for the FTIR samples had to be about 2 $mm$ to obtain good transmission. In order to increase their transparency for the spectroscopy measurements, the samples were manually grinded on a Struers grinding machine. Silicon carbide paper in the following order of roughness was used as grinding material: 320, 500, 800, 1200, 2400, 4000. The thickness variation of a sample after grinding was kept below 0.1 $mm$.

### 3.3.3 Microscope samples

The samples that were to be studied in the optical microscopes had to be polished to increase the transparency and get good images. The polishing was done after the samples had been scanned in

the X-ray tomography scanner. The samples were first embodied into an Epofix resin to be able to do automatic polishing and to prevent crack formation and cristobalite flake-off. The quartz cubes were placed in forms with the cross-section facing downwards before a ratio of 25:3 of resin and hardener were mixed together and poured over the cubes until they were just covered. The forms were then placed for 10 minutes in a rough vacuum chamber to decrease the amount of air bubbles along the walls. The resin had to harden for eight hours before the samples were ready for polishing.

The quartz samples were grinded and polished on a Struers TegraPol-31. They were mounted six at a time in the sample holder as seen in Figure 16. First, a grinding program with silicon carbide paper was run. Table 2 shows how long the quartz samples were grinded on the papers of different roughness. The samples and sample holder were cleaned with soap, water and ethanol between each run.

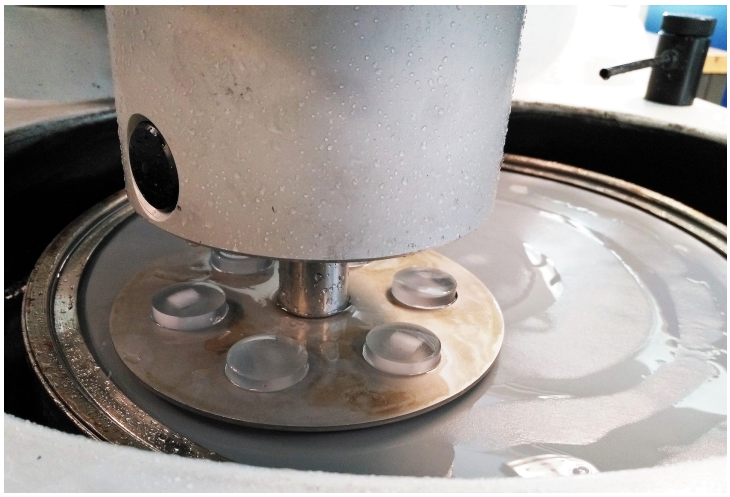

Figure 16: Embodied quartz cubes mounted for grinding on silicon carbide paper.

Table 3: Polishing time on silicon carbide paper of different roughness.

| Roughness | Polishing time [min] |
|---|---|
| 120 | 2 |
| 320 | 2 |
| 500 | 2 |
| 1200 | 2x2 |
| 2400 | 2x2 |

The samples were then polished on a Dach cloth with supply of a water based diamond suspension for 3x12.5 minutes. Between each run on the Dach cloth the samples were cleaned as described above. After the last run the samples were placed in an ultrasound bath containing ethanol for five minutes. Then the samples were polished for two minutes on a Nap-B cloth after which they were cleaned thoroughly and then dried in a hot air current.

### 3.4 Measurement and calculation of OH content

The measurement of OH content in the crucible samples was done by FTIR spectroscopy. The 2 $mm$ thin crucible slices were taped to the sample holder and placed inside the sample compartment of the FTIR spectrometer as seen in Figure 17. The spectrometer was then filled with liquid nitrogen for cooling and the sample compartment was evacuated to a pressure of about 3.5 $hPa$. For the new crucible samples the measurements were done both in the BC and the BF layer, two positions were analysed for each layer. The positions chosen were close to the middle of each layer and parallel with respect to the BC-BF border. For the used samples only the BF layer was analysed due to the low transparency of the BC layer. The heat treated samples were also analysed. For most of the heat treated samples both the BF and the BC layer could be analysed. However, some of the samples had a too high content of bubbles in their BC layer to be transparent enough.

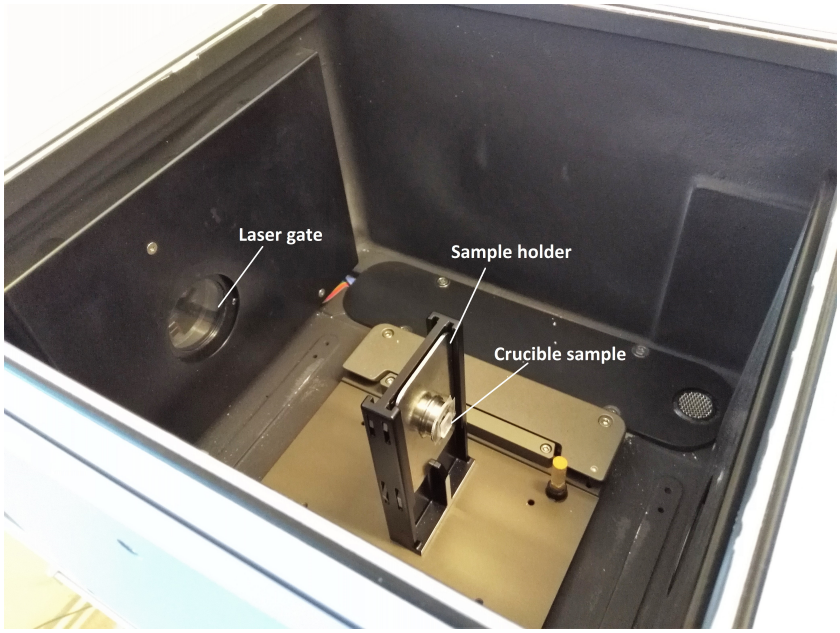


Figure 17: The FTIR spectrometer sample compartment in open position.

The calculation of the OH content from the spectroscopy raw data was done by processing the data through a script created in the computer program MATLAB. The script, which can be found in the Appendix, implements the "Philips lighting method" which is an established method for calculating low OH content in quartz glass[35]. The raw data was plotted as transmittance vs wavenumber. OH groups are characterized by absorption at wavenumbers around 3600, thus causing a drop in the transmittance at this position. The MATLAB script uses a baseline function to calculate the depth of this minima, called $T_{min}$. $T_{min}$ is then used to calculate the optical density $\beta$. The optical density is the absorbance of the light that passes through a sample and is given by Beer Lambert's law[35]:

$$\beta = \frac{1}{d} * log(\frac{1}{T_{min}}) \tag{5}$$

where $d$ is the sample thickness. The calculation of the OH content is then done by multiplying the optical density with a conversion factor:

$$OH(ppm) = \beta * factor \tag{6}$$

$$factor = \frac{M_{OH} * 10000}{eOH * p_{glass}} \tag{7}$$

where $M_{OH} = 17\ g/mol$ is the molar weight of OH, $p_{glass} = 2.21\ g\ cm^{-3}$ is the density of glass and eOH = 77.5 $L\ mol^{-1}\ cm^{-1}$ is the absorption coefficient. The OH content in each layer of each sample was calculated as the average of the two measured positions. The exception was samples with a local variation between their two positions of more than 10 $ppm$. For these samples the OH content of the two measured positions is given separately.

## 3.5 Heat treatments

### 3.5.1 Test 1

The first heat treatment was performed in a muffle furnace. Two quartz crucible rods, 4 and 7 $cm$ in length, were placed in two separate quartz container crucibles with height and diameter of 6 and 4 $cm$, respectively. Silicon feedstock was poured around the quartz rods to simulate the conditions of a real crystal pulling situation. As can be seen in Figure 18, two different kinds of silicon feedstock were used. The first type was granular silicon of high purity. This was poured into one of the container crucibles. The other was a silicon powder of slightly lower purity. This was poured into the other crucible. Due to uncertainty on whether the container crucibles would withstand the test conditions, the first test was performed in a muffle furnace instead of the VGF furnace. The muffle furnace has the advantage of a larger furnace chamber and the container crucibles could thus be placed inside Alumina containers in case of crack formation and leakage of silicon. The temperature was set to 1500 °C and the samples were held at this temperature for about two hours before being cooled down overnight.

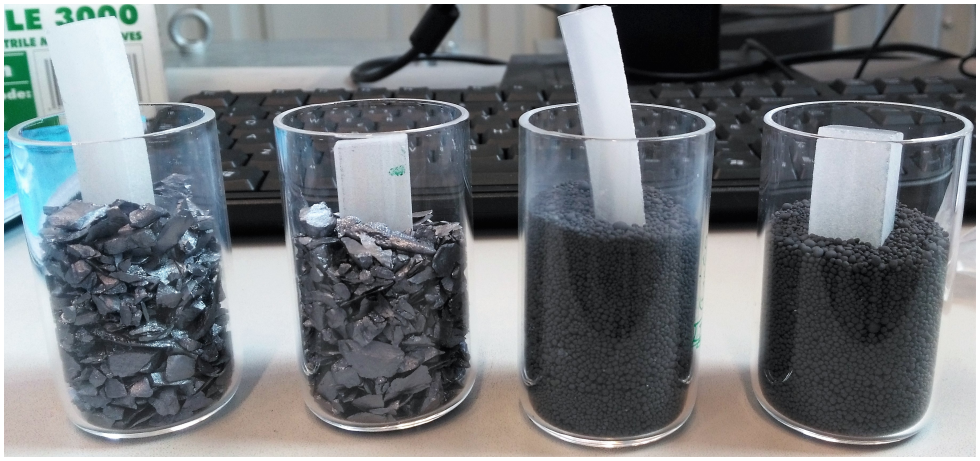

Figure 18: Container crucibles filled with granular (left) and finer (right) silicon feedstock used in Test 1 and 2.

### 3.5.2 Test 2

Due to no leakage in Test 1, the next samples were heat treated in the VGF furnace as seen in Figure 19. The VGF furnace utilizes the concept of vertical gradient freeze (VGF), meaning a vertical temperature gradient throughout the furnace. One heating element is placed directly beneath the samples and one is placed above. Two quartz rods, 8 and 5 *cm* in length, were placed in two separate container crucibles as in Test 1. The same fine and coarse silicon feedstock were used. The crucibles were placed in the oven and graphite elements were placed around. The furnace was then evacuated down to a pressure of 2 *mbar*. After a leak check to ensure a stable vacuum, argon was let into the system to create an inert Argon atmosphere of 1 *bar*. The following temperature program was run:

Table 4: Temperature program for Test 2 (1.5 h heat treatment) including ramping and dwell time for both the upper and lower heating element (HE).

| | Step | Temperature [°C] | Ramp [°C/h] | Dwell [min] |
|---|---|---|---|---|
| Upper HE | 0 | 1500 | 1200 | 2 |
| | 1 | 1450 | 600 | 90 |
| | 2 | 1383 | 10 | 2 |
| | 3 | 1 | 250 | 1 |
| | 4 | 2 | 250 | 6000 |
| Lower HE | 0 | 1500 | 1200 | 2 |
| | 1 | 1450 | 1200 | 52 |
| | 2 | 750 | 75 | 166 |
| | 3 | 1 | 250 | 1 |
| | 4 | 2 | 250 | 6000 |


Figure 19: VGF furnace in open position.

### 3.5.3 Test 3

Test 3 was run in the VGF furnace with four test crucibles for a more homogeneous heat distribution. Two of the quartz rods were 5 *cm* long while the other two had a length of 4 *cm*. The same silicon feedstock was used as in the previous tests, i.e. two crucibles were filled with the granular silicon and the other two with the finer silicon. Due to insufficient melting of the silicon in Test 2, the temperature and holding time were increased in Test 3. The details can be found in Table 5.

### 3.5.4 Heat treatments

With the ideal run conditions established, the main heat treatment experiments could be performed. The following crucible samples were heat treated in the 1.5 h run in the VGF furnace: STD_C, A_C, A_NC, B_C and B_NC. All sample rods were 5 *cm* in length and only the coarser silicon feedstock was used. The same preparation procedure was followed as described above and the same temperature program was run as in Test 3. Rods of the same crucible samples were also heat treated for 10 hours and 24 hours, the only difference being the temperature dwell time in step 1. For the 10 hour experiment the holding time was increased to 600 minutes and 550 minutes for

Table 5: Temperature program for 1.5 h heat treatment including ramping and dwell time for both the upper and lower heating element (HE).

| | Step | Temperature [°C] | Ramp [°C/h] | Dwell [min] |
|---|---|---|---|---|
| Upper HE | 0 | 1550 | 1200 | 2 |
| | 1 | 1550 | 600 | 90 |
| | 2 | 1483 | 10 | 2 |
| | 3 | 1 | 250 | 1 |
| | 4 | 2 | 250 | 6000 |
| Lower HE | 0 | 1550 | 1200 | 2 |
| | 1 | 1450 | 1200 | 72 |
| | 2 | 750 | 75 | 166 |
| | 3 | 1 | 250 | 1 |
| | 4 | 2 | 250 | 6000 |

the upper and lower heating element, respectively. For the 24 hour experiment the holding time was 1440 minutes and 1325 minutes for the upper and lower heating elements, respectively. The heat treated sample rods covered in solidified silicon were then prepared for X-ray tomography. The silicon covered samples together with what was left of the container crucible were cast into an Epofix resin to prevent the silicon from crumbling apart during sawing. Then, cubes were cut with the coarse diamond blade saw so that only a thin layer of silicon covered the quartz rod. The part of the quartz rod that was not covered in silicon was cut with the Accutom saw into cubes as previously described.

### 3.5.5 Czochralski puller experiment

Due to a damage on the heating elements in the VGF furnace it was decided to perform a complementary 10 hour heat treatment in the Czochralski puller as seen in Figure 20.

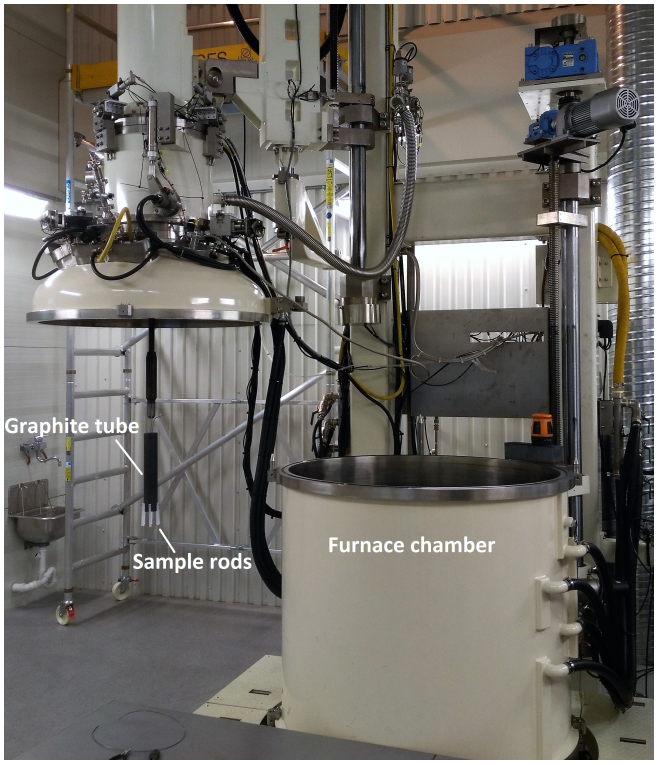


Figure 20: Czochralski puller with the furnace chamber in open position. The seed with the graphite rod and the crucible rods are hanging from the upper housing to the left.

Only two crucible types were prepared for the experiment, STD_C and A_C, due to lack of crucible B material. Three rods of 10 $cm$ length and 1 $cm$ width were cut from each crucible. The rods were then attached to the end of a 30 $cm$ long graphite tube with molybdenum wire going through holes in the tube. The holes were made by drilling through the graphite. As seen in Figure 21 and 22, the rods were attached so that most of their length, 7 $cm$ in total, hung below the graphite tube. The graphite tube was then attached to the seed of the puller with a thicker molybdenum wire before the seed and tube were hoisted up into the upper housing. The crucible was filled with 15 $kg$ of small sized Hemloch silicon before the furnace chamber was sealed. The air was then pumped out of the chamber until a vacuum of 5 $Pa$ was reached. A leak check was performed to ensure a stable vacuum before argon gas was introduced into the furnace chamber from above. The pressure stabilized at around 2000 $Pa$. The power was then turned on and the crucible was made to rotate with 1 $rpm$. The temperature stabilized at 1500 °C. After about six hours all the silicon had melted and the crucible rods could be lowered into the melt. They were lowered with a speed of 50 $mm/min$ until the melt covered 2.6 $cm$ of their total length.

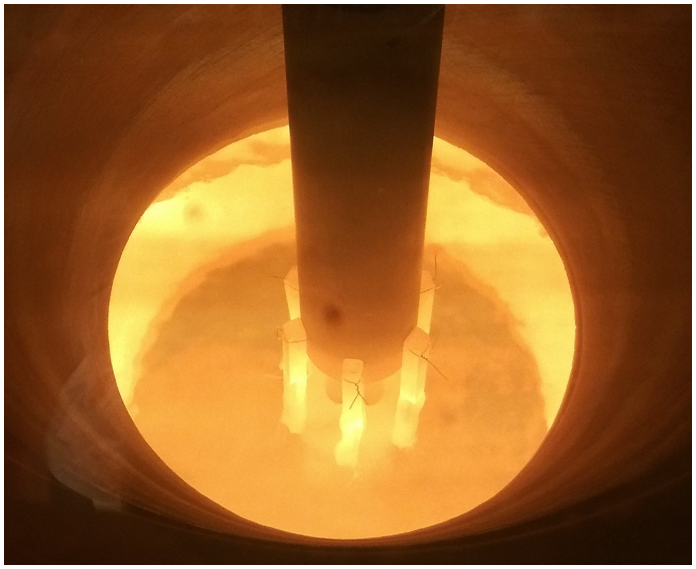

Figure 21: Picture of crucible rods being lowered into the silicon melt.

The rods were held in this position for 10 hours before being pulled up from the melt. The rods were then kept at a position just above the shield for 30 minutes before being pulled up above the shutter were they were kept for another 30 minutes. Then the furnace chamber was sealed off and the upper housing was detached from the chamber. The seed was lowered and the rods could be detached from the graphite rod. As seen in Figure 22 the rods were then cut into four pieces for further analysis, two from the part that had been covered with melt (Position 1 and 2) and two from the part above (Position 3 and 4).

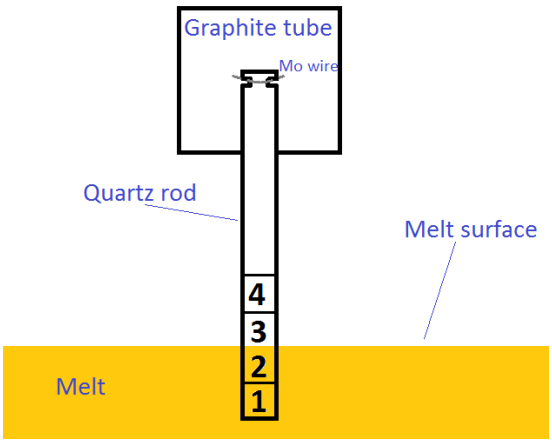


Figure 22: Illustration of the four positions of the samples collected from the quartz rods after the Czochralski experiment.

A temperature simulation was run by a SINTEF researcher using the simulation program CGSim[40]. The simulation gives an overview of, among other things, the temperature distribution in the silicon melt and quartz crucible rods. The simulation was run with a crucible rotation of 1 $rpm$, heater power of 78 $kW$, silicon feedstock of 20 $kg$. The average melt temperature was 1493 °C.

## 3.6 X-ray tomography

The X-ray scanning of the samples was done in a Nikon XT H 225 ST X-ray computed tomography scanner. Each quartz cube was placed on a sample holder about 5 $cm$ from the X-ray source with the BC layer facing downwards. The Wolfram X-ray source generated X-rays at 180 $kV$ and 110 $\mu A$. The cube was scanned for about 50 minutes while completing one rotation to obtain pictures from every angle. Every third hour, between a sample change, a shading correction must be performed to compensate for changes in the background. The raw data were then uploaded to the computer program "CT Pro 3D" for 3D reconstruction. The program allowed for some choices regarding image quality. The reconstruction resulted in a stack of about 1400 TIFF pictures for each quartz cube sample showing the cross-section throughout the sample when starting at the beginning of the BC layer and moving towards the end of the BF layer. An example of one slice from the cross-section of the BC layer of crucible STD can be seen in Figure 23.

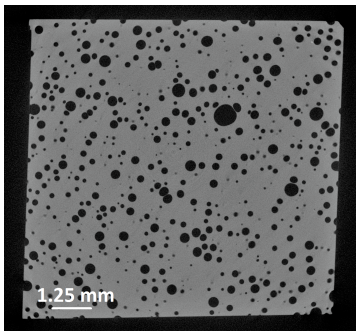


Figure 23: X-ray tomography reconstruction of one slice of the cross-section in the BC layer of a used STD crucible.

## 3.7 Analysis of bubble content with ImageJ

The bubble content in the scanned quartz cubes was determined by uploading the stack of cross-sections to the computer program "ImageJ". A script was used to calculate the bubble percent per area for each slice. This is the same script that was used in the Project work and can be found in the Appendix. The bubble percent per slice is automatically added together by the script to get a mean bubble volume percent for the whole cubic crucible sample. In order for the script to work, the exact area of the cross-section that is to be measured must be delineated. Furthermore, the color threshold and contrast had to be adjusted for to separate the bubbles from the quartz background. The calculated bubble percent for each slice was then uploaded to Microsoft Excel where graphs were plotted for every scanned sample. The plots show the bubble percent per area as a function of the position in the cubic sample in millimetre when starting at the outer part of the BC layer and moving towards the outer part of the BF layer. The plots for the new and used

crucibles display the mean value of Series 1 and 2. For the heat treated samples only one series exist per sample. The mean bubble percent for the whole cubic crucible sample could be directly read out from the script results. The mean bubble percent of the BC and the BF layer considered separately was also calculated. This was done by summing together the bubble percent per area for every slice in the respective layers and then divide this by the number of slices. A cut-off value in bubble percent per area had to be chosen to separate the two layers from each other. For the new and heat-treated crucibles the cut-off value was set to 0.05 %. Thus, every slice with a bubble percent below this value is considered to be part of the BF layer and every slice with a value above is considered to be part of the BC layer. For the used crucibles the cut-off values vary. These are found by looking at the min values that the graphs in Figure 26 to 28 obtain at the BC-BF border before they start to increase again when moving further into the BF layer, i.e. the smallest minimum directly after the BC-BF transition.

The ImageJ plugin "BoneJ" was used to find the bubble distribution in the crucible samples. The plugin works by the same principle as the script described above, but in addition it numerates each bubble and adds the slices for the separate bubbles together to get the volume per bubble. The plugin was used to obtain a picture for every sample where each cross-section of a sample is put on top of each other. I.e. all the bubbles in one sample are projected onto one slice. Colours were added to differentiate between the size of the bubbles. The further the color is shifted towards the blue end of the spectrum, the smaller the bubble volume is, and vice versa, the further towards the red end of the spectrum the larger the bubble volume.

## 3.8 Optical microscopy

### 3.8.1 Picturing crucible cross-sections

A Leica MEF4M reflection optical microscope was used to take pictures of the cross-sections of the polished crucible samples. Seven to eight pictures were taken per sample at 5x resolution, from the inner to the outer crucible layer. The pictures for each sample were then aligned and stitched together to give an enlarged image of the crucible cross-section. One cross-section covers a real area of about 2x10 = 20 $mm^2$, i.e. 20 % of the sample width is accounted for.

### 3.8.2 Bubble counting with transmission light microscope

A Leitz METALLUX 3 transmission light microscope was used to count bubbles in the BF layer with diameter smaller than 9 $\mu m$ as this is the detection limit of the X-ray tomography scanner. An objective with 20x magnification was used to zoom in on the cubic samples so that the gap between lens and sample became as small as possible. This corresponded to a sample depth of about 0.9 $mm$. Then each interior plane of the sample was scanned visually and the sub 9 $\mu m$ bubbles were counted. After a plane had been scanned, the image was zoomed out to reach the next plane by turning the magnification knob 45° while searching for any bubbles that may have been in between the planes. The total volume scanned for each sample was approximately 1 $cm$ x 0.4 $cm$ x 0.09 $cm$ = 0.036 $cm^3$. Bubbles within 2 $mm$ to the outer part of the BF layer (close to the crucible-melt interface) were accounted for separately. Furthermore, an objective with 2.5x magnification was used to count the number of bubble lines in the whole BF layer sample volume. A bubble line is defined here as four or more bubbles positioned linearly, in close proximity with respect to each other and parallel to the crucible-melt interface.

# 4 Results

## 4.1 X-ray tomography data

Figure 24 to 28 show plots of bubble percent per area for every slice of the crucible sample versus position for the new, industrially used and samples heat treated in this work, respectively. The measurements start at the beginning of the BC layer and end at the outermost part of the BF layer. The plots for the new and used samples are representing the calculated mean values of the bubble percent of Series 1 and 2. The heat treated samples are based on values from one series only. "melt" and "top" refers to whether the sample was inside or outside the silicon melt, respectively. For the Czochralski heat treated samples "bottom" refers to Position 1 deepest inside the silicon melt. Table 6 gives the mean value of the bubble volume percent of the BC and BF layer combined as well as for both layers separately for the new crucibles of Series 1 and 2. Table 7 gives the corresponding information for the used crucible samples and Table 8 to 11 give the bubble volume percent for the heat treated samples. Table 12 gives the bubble volume percent for the new and used crucible samples investigated in my Project work[4]. These are mean values of three series.

### 4.1.1 Plots of bubble percent per area

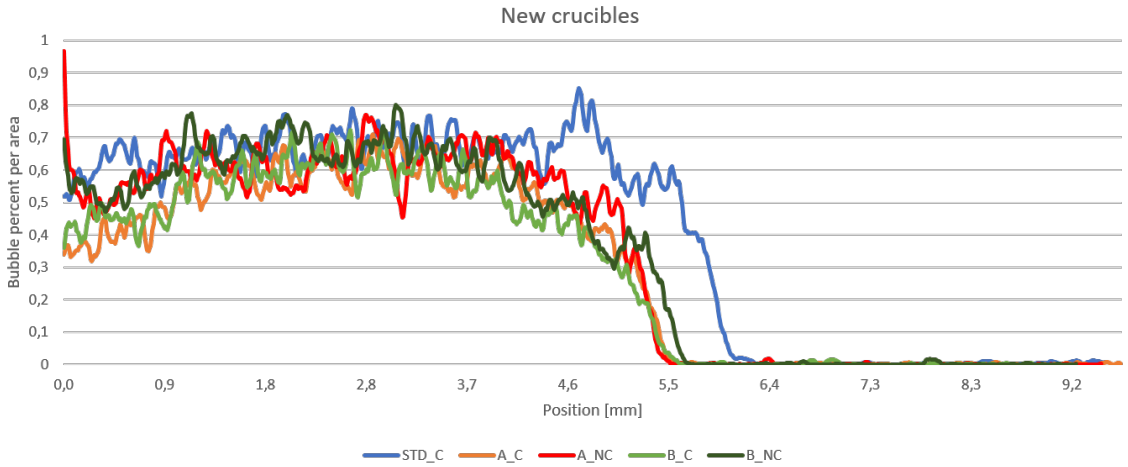


Figure 24: Mean plots of Series 1 and 2 showing bubble percent per area as a function of position for the new crucibles when starting at the beginning of the BC layer.

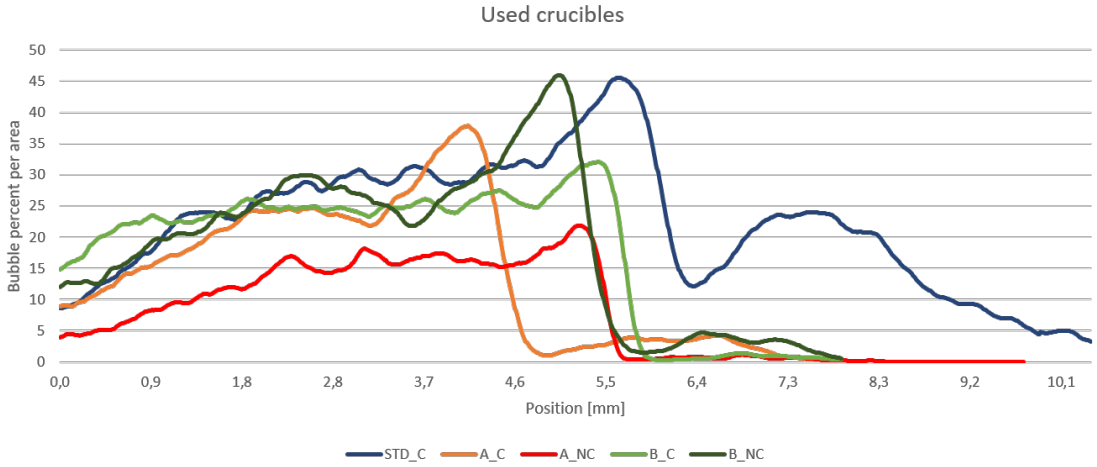


Figure 25: Mean plots of Series 1 and 2 showing bubble percent per area as a function of position for the used crucibles when starting at the beginning of the BC layer.

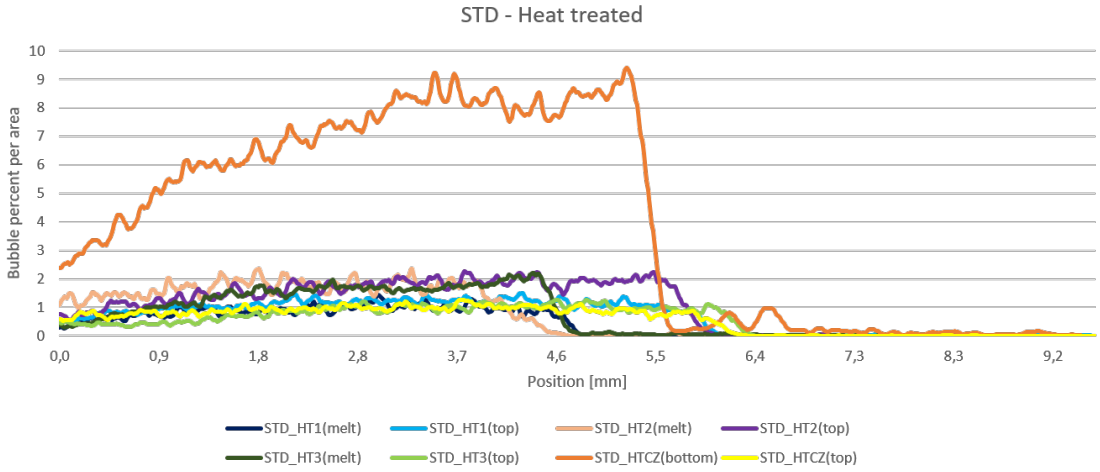


Figure 26: Plots showing bubble percent per area as a function of position for the heat treated STD crucible when starting at the beginning of the BC layer.

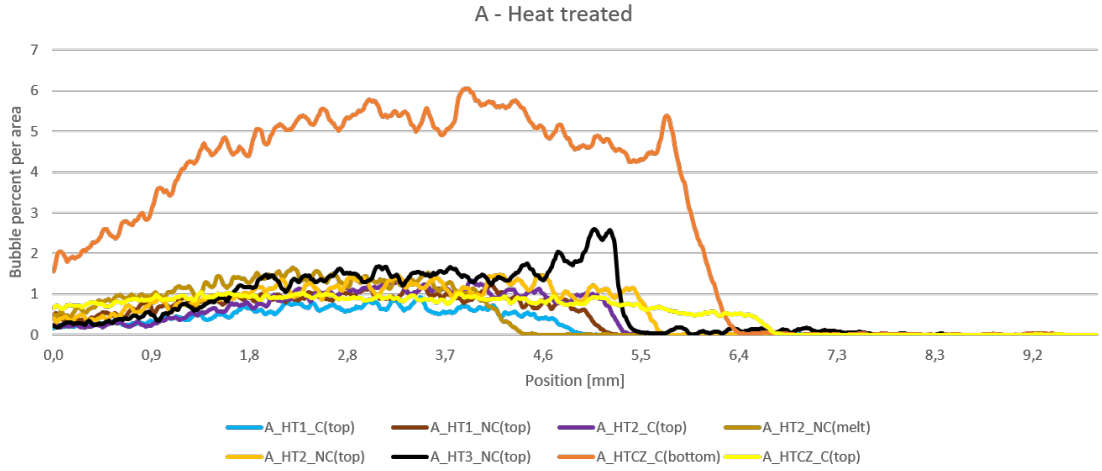


Figure 27: Plots showing bubble percent per area as a function of position for the heat treated A crucible when starting at the beginning of the BC layer.

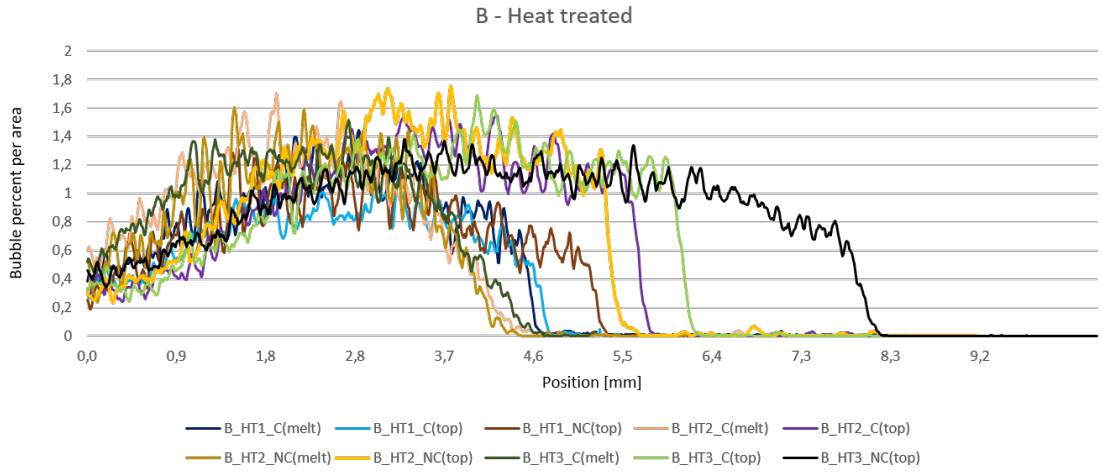


Figure 28: Plots showing bubble percent per area as a function of position for the heat treated B crucible when starting at the beginning of the BC layer.

#### 4.1.2 Bubble volume percent of crucible layers

Table 6: Bubble volume percent of the new crucibles for both layers combined and the BC and the BF layer separately. Mean value of Series 1 and 2.

| New crucible | Both layers [%] | BC layer [%] | BF layer [%] |
|---|---|---|---|
| STD_C | 0.41 | 0.63 | 0.0042 |
| A_NC | 0.33 | 0.58 | 0.0020 |
| A_C | 0.29 | 0.51 | 0.0019 |
| B_NC | 0.35 | 0.57 | 0.0021 |
| B_C | 0.32 | 0.51 | 0.0028 |

Table 7: Bubble volume percent of the used crucibles for both layers combined and the BC and the BF layer separately. Mean value of Series 1 and 2.

| Used crucible | Both layers [%] | BC layer [%] | BF layer [%] |
|---|---|---|---|
| STD_C | 22.7 | 27.3 | 14.3 |
| A_NC | 7.9 | 13.4 | 0.38 |
| A_C | 12.7 | 21.4 | 1.94 |
| B_NC | 16.1 | 24.7 | 1.72 |
| B_C | 16.6 | 24.0 | 0.55 |

Table 8: Bubble volume percent of the 1.5 h heat treated crucibles for both layers combined and the BC and the BF layer separately.

| Heat treated 1.5 h | Both layers [%] | BC layer [%] | BF layer [%] |
|---|---|---|---|
| STD_C_melt | 0.51 | 0.86 | 0.0043 |
| STD_C_top | 0.68 | 1.07 | 0.0090 |
| A_C_top | 0.27 | 0.51 | 0.0017 |
| A_NC_melt | - | - | - |
| A_NC_top | 0.45 | 0.80 | 0.0024 |
| B_C_melt | 0.51 | 0.88 | 0.0102 |
| B_C_top | 0.36 | 0.71 | 0.0022 |
| B_NC_melt | - | - | - |
| B_NC_top | 0.46 | 0.78 | 0.0011 |

Table 9: Bubble volume percent of the 10 h heat treated crucibles for both layers combined and the BC and the BF layer separately.

| Heat treated 10 h | Both layers [%] | BC layer [%] | BF layer [%] |
|---|---|---|---|
| STD_C_melt | 1.02 | 1.54 | 0.0131 |
| STD_C_top | 1.05 | 1.58 | 0.0170 |
| A_C_top | 0.47 | 0.79 | 0.0021 |
| A_NC_melt | 0.67 | 1.10 | 0.0054 |
| A_NC_top | 0.60 | 0.98 | 0.0023 |
| B_C_melt | 0.60 | 0.97 | 0.0067 |
| B_C_top | 0.58 | 0.97 | 0.0029 |
| B_NC_melt | 0.65 | 0.93 | 0.0057 |
| B_NC_top | 0.65 | 1.05 | 0.0070 |

Table 10: Bubble volume percent of the 24 h heat treated crucibles for both layers combined and the BC and the BF layer separately. *All are wall samples except for B_NC which is a corner sample due to lack of wall material.

| Heat treated 24 h | Both layers [%] | BC layer [%] | BF layer [%] |
|---|---|---|---|
| STD_C_melt | 0.88 | 1.37 | 0.0441 |
| STD_C_top | 0.59 | 0.83 | 0.0030 |
| A_NC_melt | - | - | - |
| A_NC_top | 0.74 | 1.17 | 0.0588 |
| B_C_melt | 0.82 | 0.95 | 0.0088 |
| B_C_top | 0.70 | 0.97 | 0.0029 |
| B_NC_melt* | - | - | - |
| B_NC_top* | 0.71 | 0.93 | 0.0007 |

Table 11: Bubble volume percent of the heat treated crucibles from the Czochralski experiment for both layers combined and the BC and the BF layer separately.

| Heat treated CZ | Both layers [%] | BC layer [%] | BF layer [%] |
|---|---|---|---|
| STD_C_bottom | 4.07 | 6.56 | 0.2147 |
| STD_C_top | 0.57 | 0.87 | 0.0051 |
| A_C_bottom | 2.85 | 4.45 | 0.0187 |
| A_C_top | 0.52 | 0.75 | 0.0028 |

Table 12: Bubble volume percent of the Project Work (PW) crucibles for both layers combined and the BC and the BF layer separately. Mean value of three series.

| PW crucible | Both layers [%] | BC layer [%] | BF layer [%] |
|---|---|---|---|
| STD_new | 0.33 | 0.58 | 0.0033 |
| STD_used | 13.2 | 20.4 | 0.37 |
| A_new | 0.27 | 0.53 | 0.0032 |
| A_used | 13.8 | 21.4 | 2.3 |
| B_new | 0.37 | 0.59 | 0.0024 |
| B_used | 15.1 | 20.8 | 0.39 |

## 4.2 Temperature simulation of Czochralski experiment

Figure 29 gives the temperature vs position in the crucible rods as simulated from the Czochralski experiment when starting in the silicon melt (Position 1) and moving towards the top part outside the melt (Position 4). Figure 30 shows the temperature distribution in a cross-section of both the sample rod and the interior of the crucible[40].

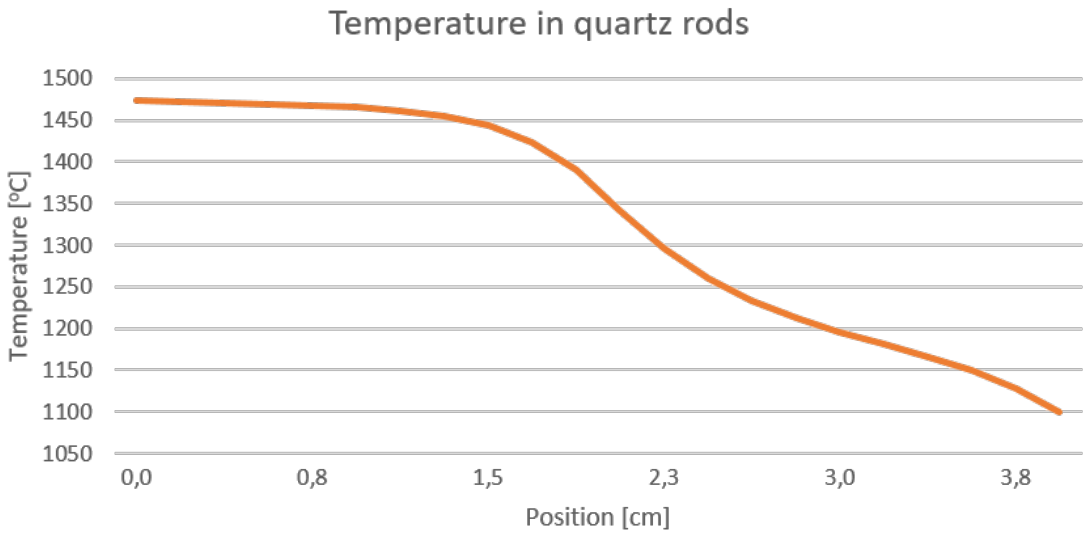


Figure 29: Simulated temperature in the quartz rods from the Czochralski experiment plotted versus the position in the rod when starting at Position 1 inside the melt[40].

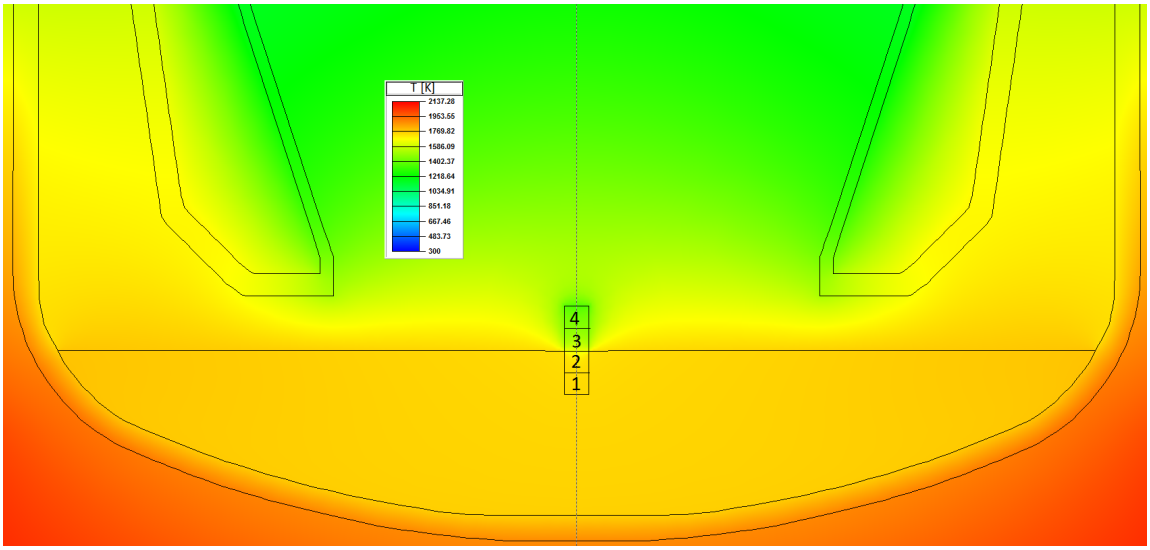


Figure 30: Cross-section of the crucible and sample rod showing the temperature distribution as simulated from the Czochralski experiment[40].

## 4.3 OH content

Figure 31 gives the OH content in ppm measured by FTIR spectroscopy for the new, used and VGF heat treated samples. The results are plotted as OH content versus heat treatment, with increasing holding time along the x-axis. Table 13 to 18 give the same information as Figure 31. However, in the tables it is possible to distinguish between the coated and non-coated samples for crucibles of the same type. The tables also include the results from the corner positions of the new and industrially used crucibles in addition to the OH content of the samples heat treated in the Czochralski puller. The OH values are calculated from the average of two positions in each sample. For the samples where two values are given with a slash in between, the variation in OH content between the two positions is exceeding 10 ppm.

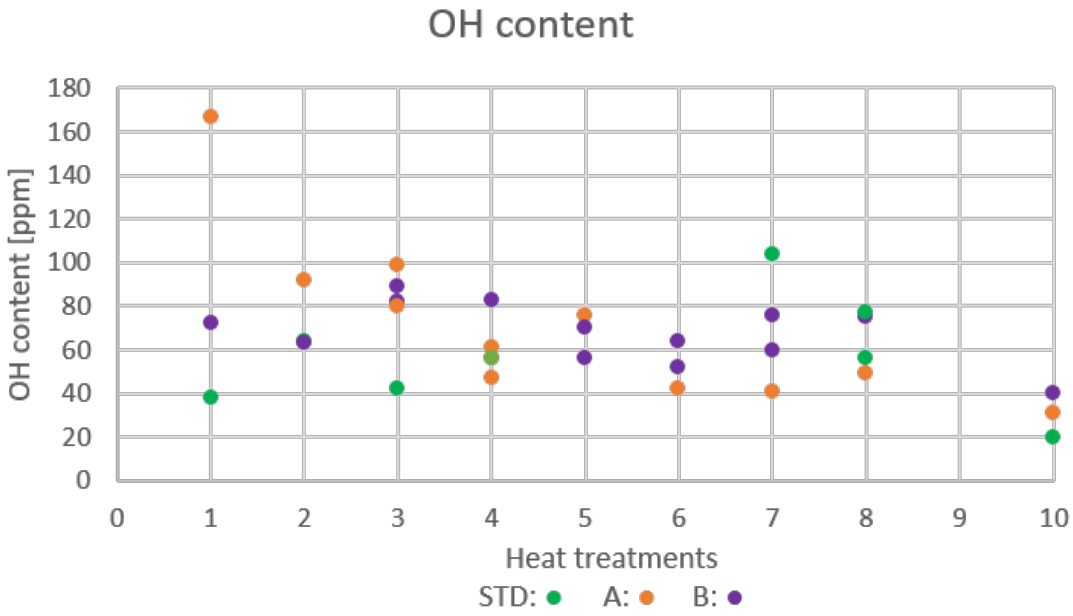


Figure 31: Plot of the OH content in ppm for the new, VGF heat-treated and used crucible samples. The heat treatments along the x-axis are listed in the following order: 1: new_BC, 2: new_BF, 3: 1.5h_BC, 4: 1.5h_BF, 5: 10h_BC, 6: 10h_BF, 7: 24h_BC, 8: 24h_BF, 10: used_BF.

Table 13: OH content in ppm for the new crucible samples.

| Sample | OH content [*ppm*] |
|---|---|
| STD_corner_BC | 40 |
| STD_corner_BF | 36 |
| STD_wall_BC | 38 |
| STD_wall_BF | 64 |
| A_corner_BC | 106 |
| A_corner_BF | 60 |
| A_wall_BC | 167 |
| A_wall_BF | 92 |
| B_corner_BC | 85 |
| B_corner_BF | 43 |
| B_wall_BC | 72 |
| B_wall_BF | 63 |

Table 14: OH content in ppm for the used crucible samples. BF layer only.

| Sample | OH content [*ppm*] |
|---|---|
| STD_corner_BF | 32 |
| STD_wall_BF | 20 |
| A_corner_BF | 23 |
| A_wall_BF | 31 |
| B_corner_BF | 35 |
| B_wall_BF | 30/43 |

Table 15: OH content in ppm for crucible samples undergoing 1.5 hour heat treatment. Wall positions only.

| Sample | OH content [*ppm*] |
|---|---|
| STD_C_BC | 42 |
| STD_C_BF | 56 |
| A_NC_BC | 99 |
| A_NC_BF | 47 |
| A_C_BC | 82 |
| A_C_BF | 61 |
| B_NC_BC | 80/91 |
| B_NC_BF | 83 |
| B_C_BC | 89 |
| B_C_BF | 56 |

Table 16: OH content in ppm for crucible samples undergoing 10 hours heat treatment. Wall positions only.

| Sample | OH content [*ppm*] |
|---|---|
| STD_C_BC | - |
| STD_C_BF | - |
| A_NC_BC | 76/84 |
| A_NC_BF | 42/53 |
| B_NC_BC | 56 |
| B_NC_BF | 52 |
| B_C_BC | 70 |
| B_C_BF | 64 |

Table 17: OH content in ppm for crucible samples undergoing 24 hours heat treatment. Wall positions only.

| Sample | OH content [*ppm*] |
|---|---|
| STD_C_BC | 104 |
| STD_C_BF | 56 |
| A_NC_BC | 41 |
| A_NC_BF | 49 |
| B_NC_BC | 60 |
| B_NC_BF | 75 |
| B_C_BC | 76 |
| B_C_BF | 77 |

Table 18: OH content in ppm for crucible samples from Czochralski puller experiment. All samples are coated and taken from wall positions only.

| Sample | OH content [*ppm*] |
|---|---|
| STD_BC_top | 57 |
| STD_BF_top | 64/76 |
| STD_BC_bottom | - |
| STD_BF_bottom | 49 |
| A_BC_top | 80 |
| A_BF_top | 73 |
| A_BC_bottom | 40 |
| A_BF_bottom | 63 |

## 4.4 Crucible cross-sections

Figure 32 to 40 show cross-sections of the crucible samples taken with an optical microscope at 5x magnification. Figure 32 to 36 show the cross-sections of the new and industrially used samples whereas Figure 37 to 40 show the cross-sections of the crucible samples heat-treated in this work.

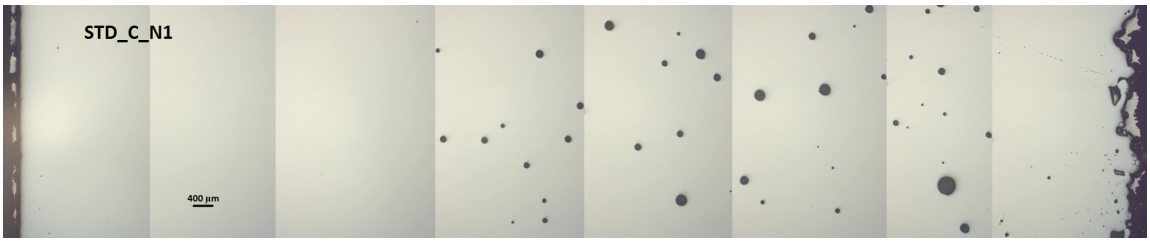


(a)

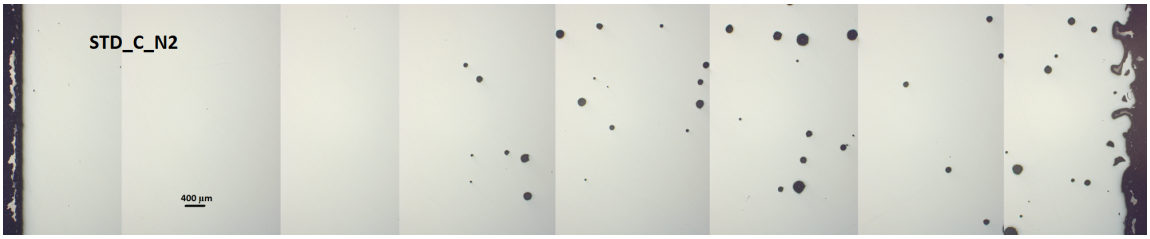


(b)

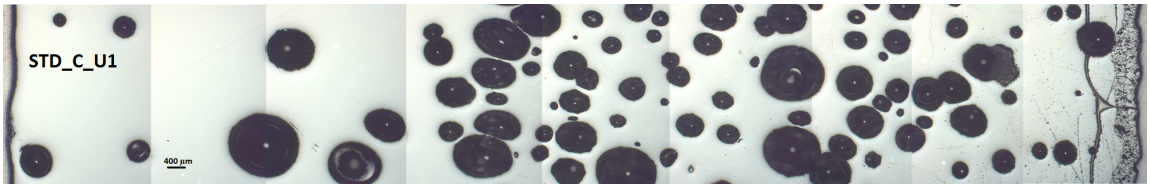


(c)

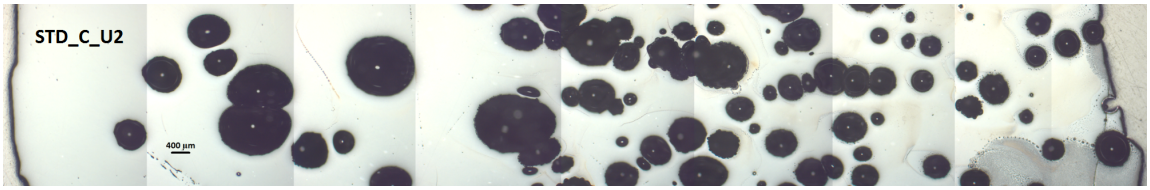


(d)

Figure 32: Optical microscope pictures of cross-sections of crucible STD for the new samples of Series 1 (32a) and Series 2 (32b) and the used samples of Series 1 (32c) and Series 2 (32d)

.

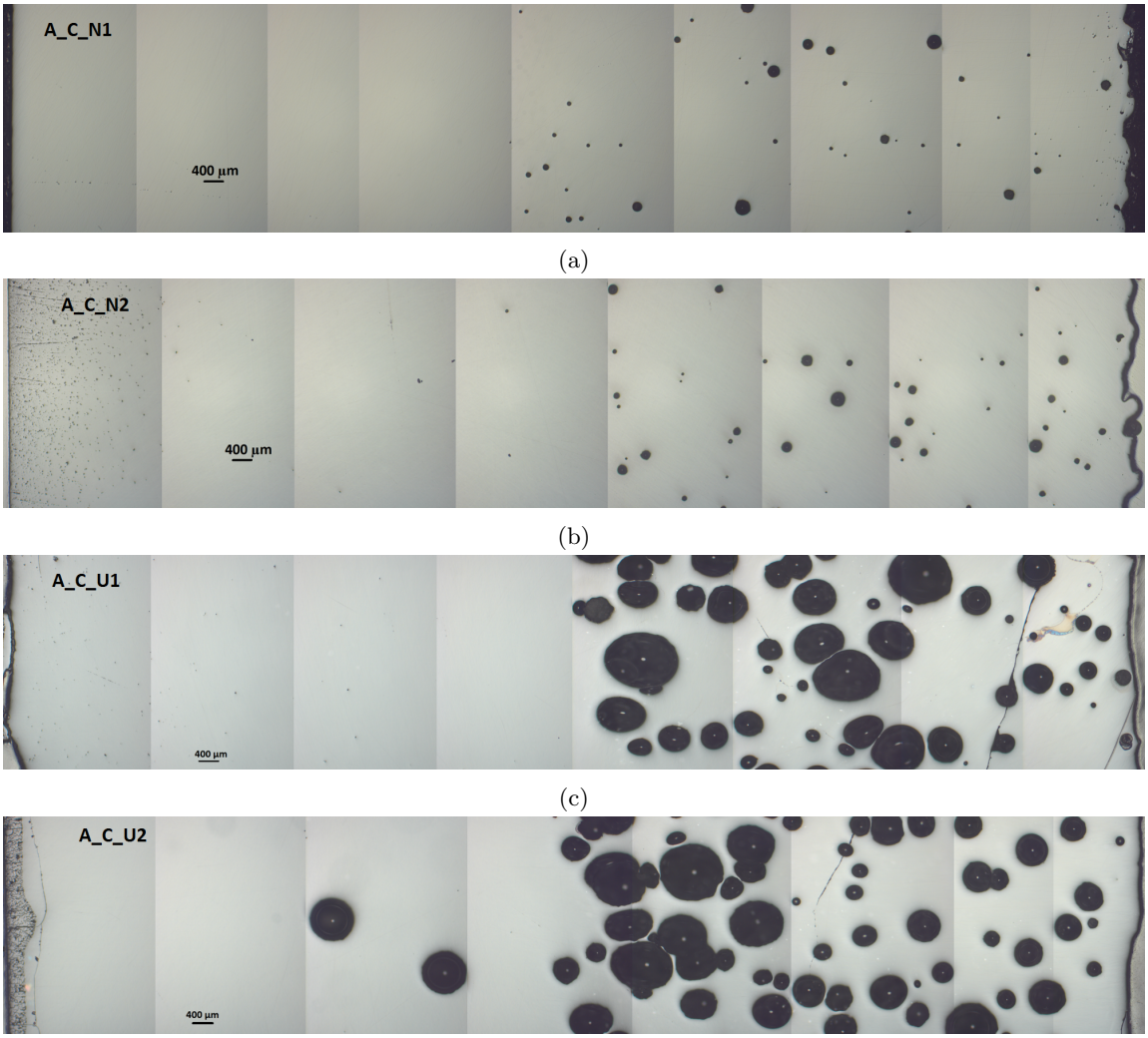


Figure 33: Optical microscope pictures of cross-sections of crucible A coated for the new samples of Series 1 (33a) and Series 2 (33b) and the used samples of Series 1 (33c) and Series 2 (33d)

.

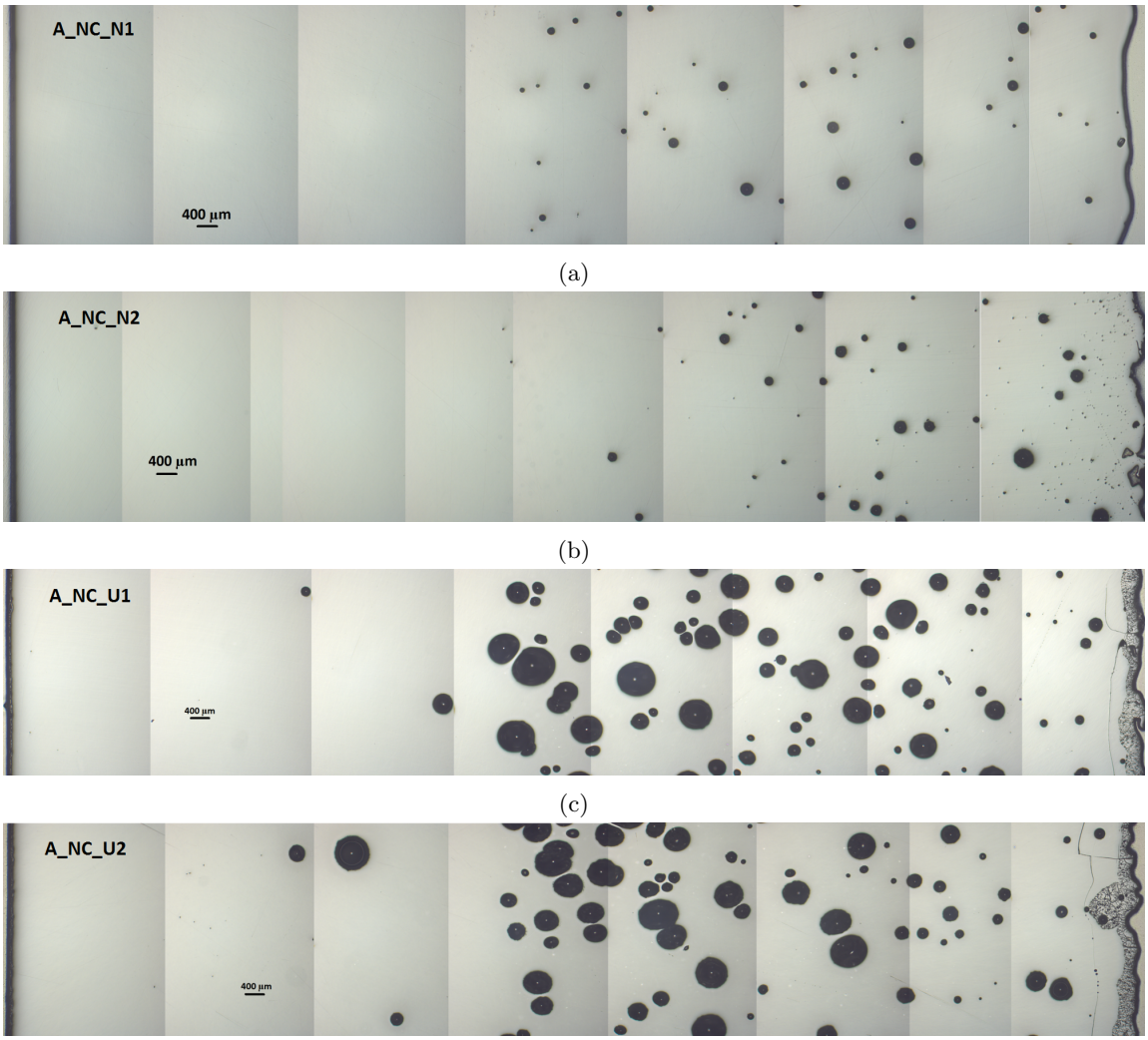


Figure 34: Optical microscope pictures of cross-sections of crucible A non-coated for the new samples of Series 1 (34a) and Series 2 (34b) and the used samples of Series 1 (34c) and Series 2 (34d)

.

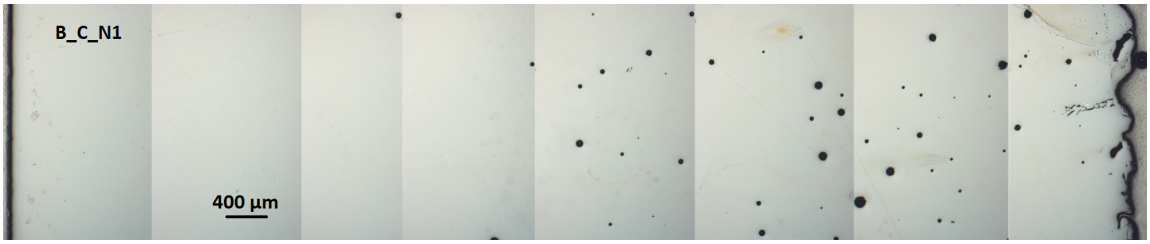


(a)

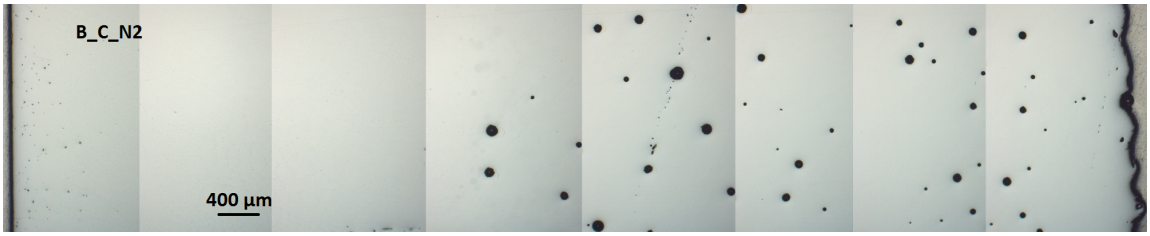


(b)

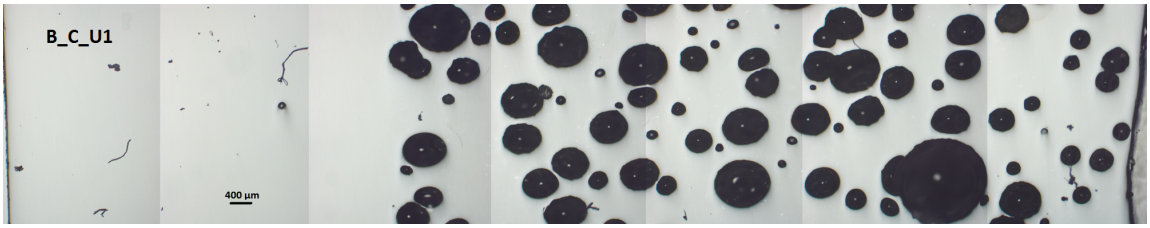


(c)

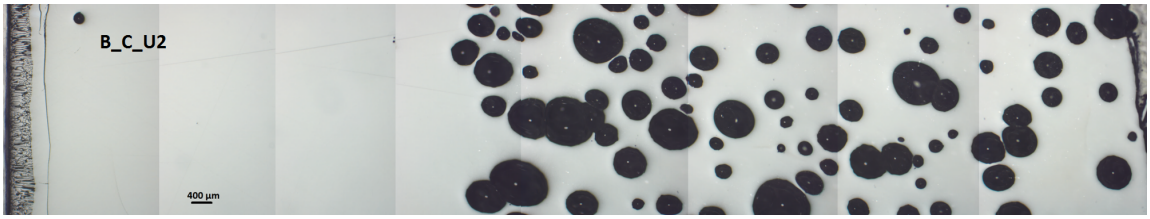


(d)

Figure 35: Optical microscope pictures of cross-sections of crucible B coated for the new samples of Series 1 (35a) and Series 2 (35b) and the used samples of Series 1 (35c) and Series 2 (35d)

.

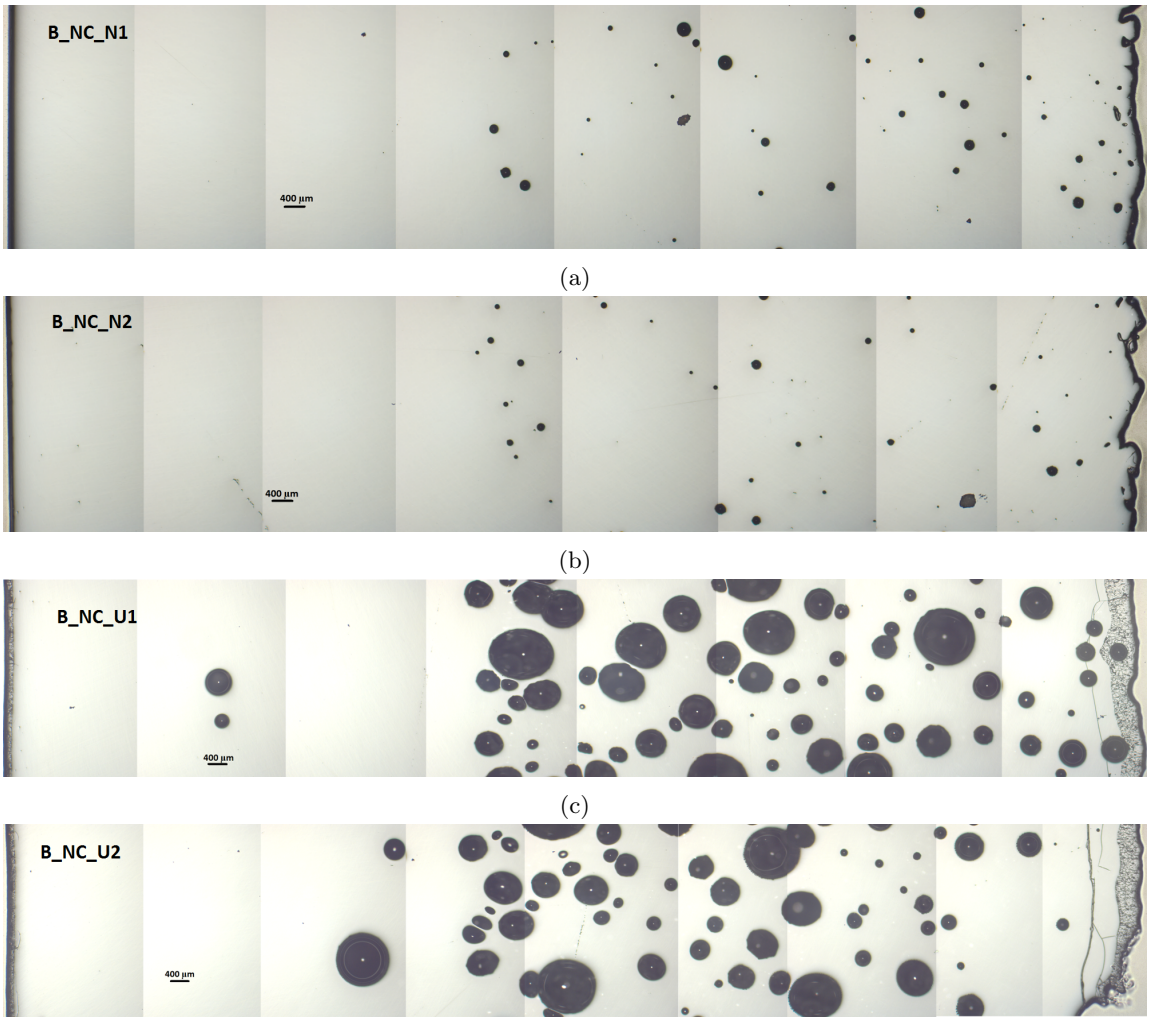


Figure 36: Optical microscope pictures of cross-sections of crucible B non-coated for the new samples of Series 1 (36a) and Series 2 (36b) and the used samples of Series 1 (36c) and Series 2 (36d)

.

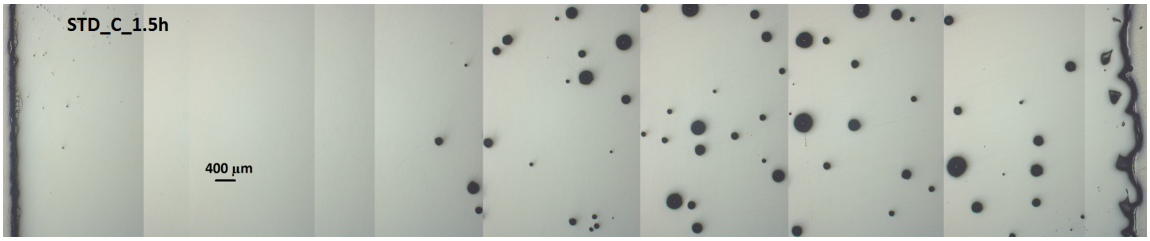


(a)

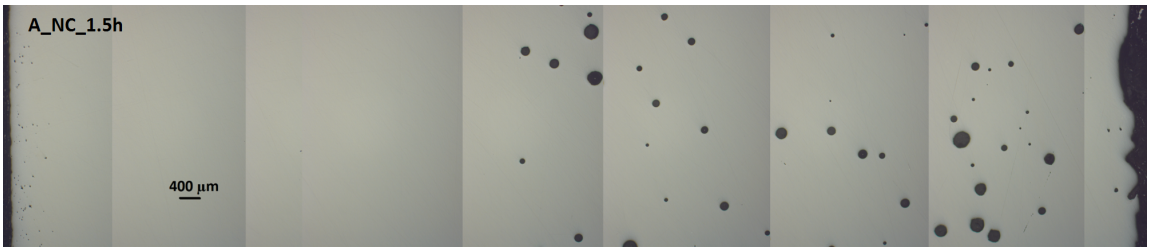


(b)

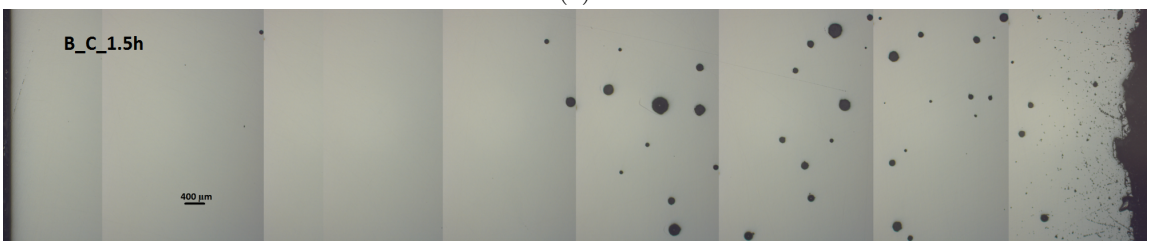


(c)

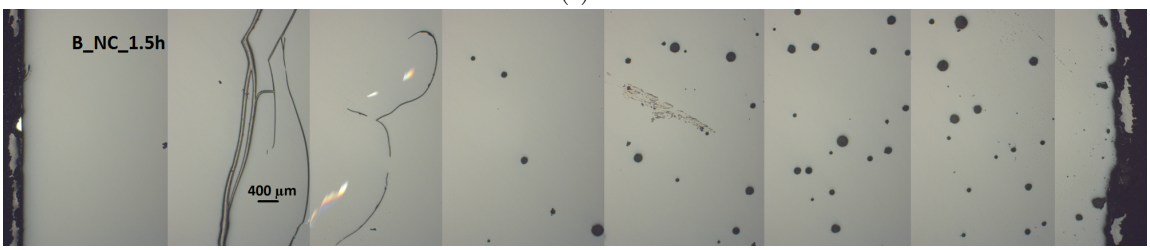


(d)

Figure 37: Optical microscope pictures of cross-sections of the crucible samples heat treated for 1.5 hour. STD_top (37a), A_C_top (37b), B_C_top (37c) and B_NC_top (37d).

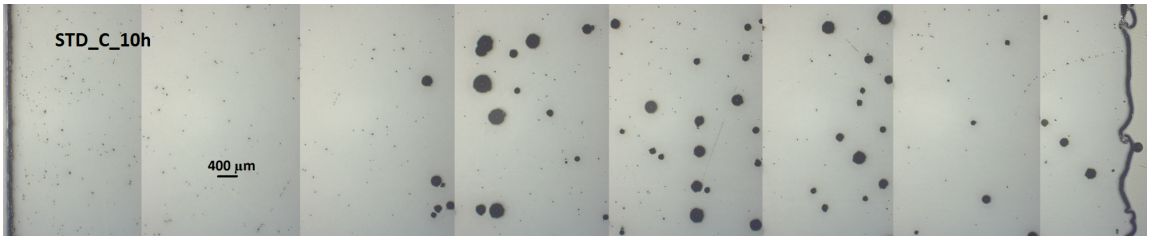


(a)

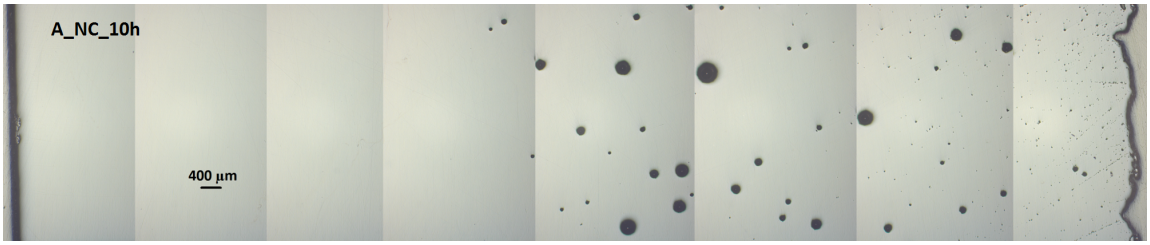


(b)

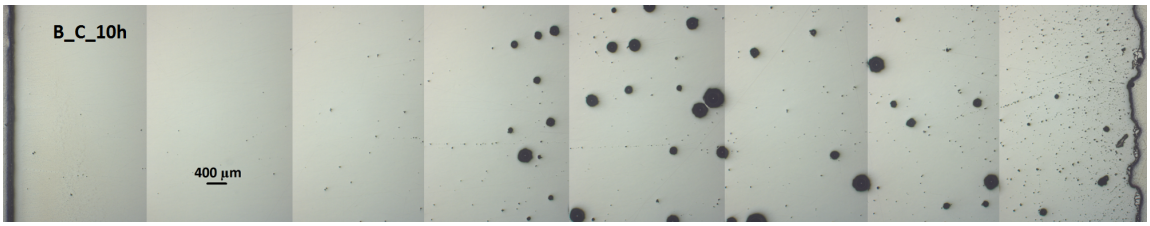


(c)

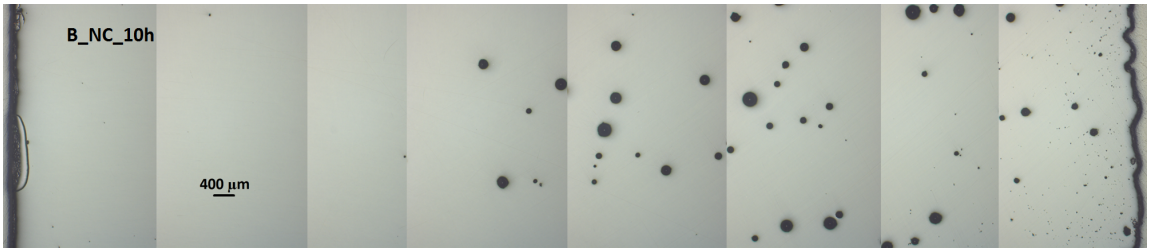


(d)

Figure 38: Optical microscope pictures of cross-sections of the crucible samples heat treated for 10 hours. STD_top (38a), A_C_top (38b), B_C_top (38c) and B_NC_top (38d).


(a)


(b)

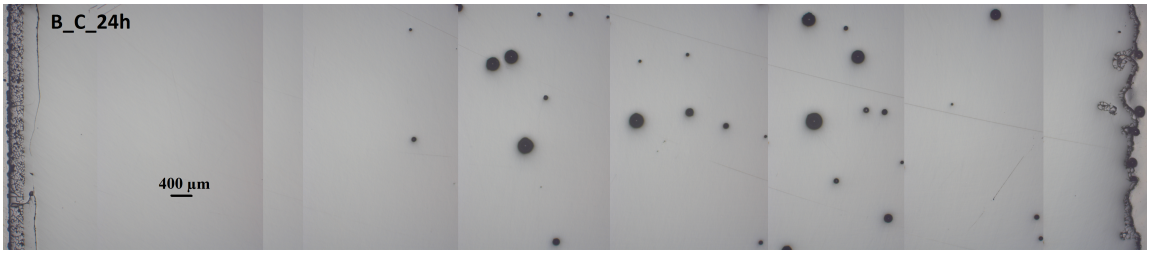


(c)

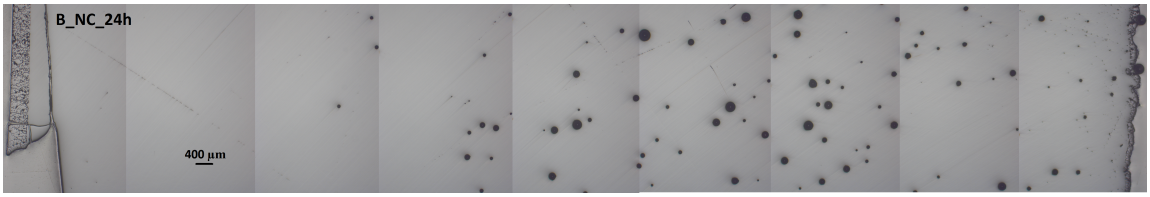


(d)

Figure 39: Optical microscope pictures of cross-sections of the crucible samples heat treated for 24 hours. STD_top (39a), A_C_top (39b), B_C_top (39c) and B_NC_top (39d).

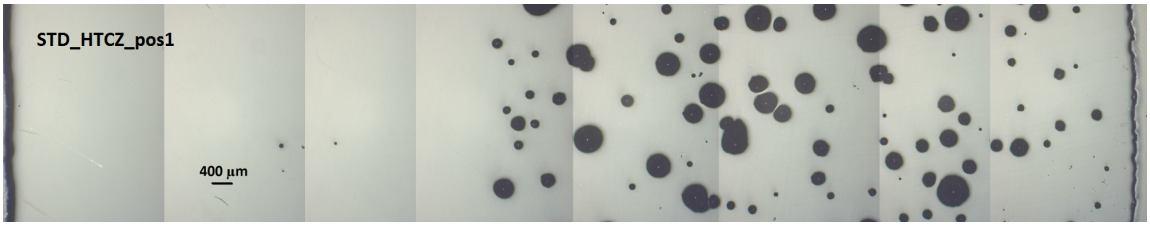


(a)

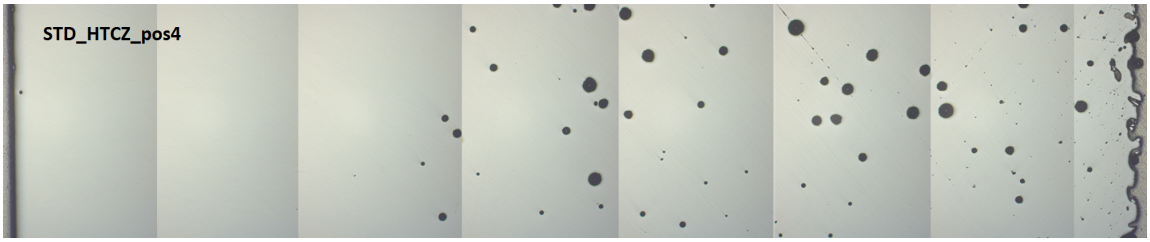


(b)

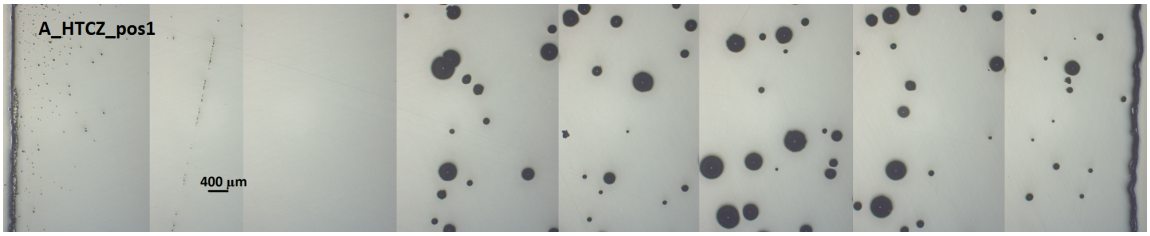


(c)

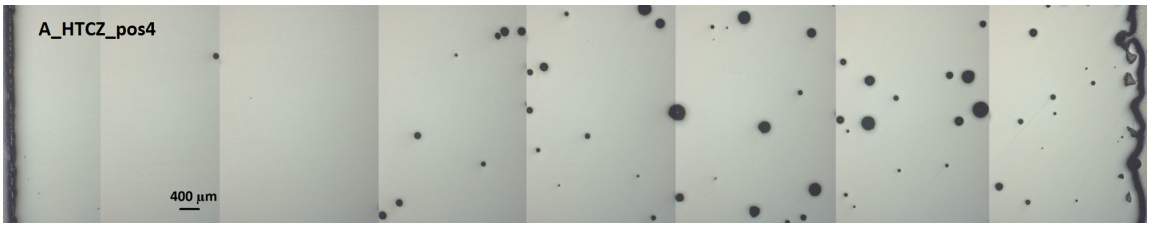


(d)

Figure 40: Optical microscope pictures of cross-sections of the crucible samples heat treated in the Czochralski puller for 10 hours. STD_bottom (40a), STD_top (40b), A_C_bottom (40c) and A_C_top (40d).

## 4.5 Bubbles below tomography detection limit

Table 19 gives the total density of bubbles with diameter smaller than the 9 $\mu m$ tomography detection limit. Furthermore, the density of these bubbles in the border region, i.e. within the 2 $mm$ closest to the crucible-melt interface, are accounted for separately. A transmission light microscope with a 20x magnification objective was used to count the bubbles by gradually defocusing through the sample. In addition, the number of bubble lines in the whole BF layer volume of each cubic sample has been counted. This corresponds to a volume of about 0.4 $cm^3$. This was done with a 2.5x magnification objective. Table 20 and 21 give the corresponding information for the used and heat-treated crucibles, respectively. Figure 41 show examples of bubble lines in a sample of the new STD crucible taken at 5x magnification.

Table 19: Density of bubbles in BF layer below tomography detection limit and number of bubble lines for the new crucible samples. Average value of two series.

| New crucible | Total density $[cm^{-3}]$ | Border region density $[cm^{-3}]$ | Bubble lines |
|---|---|---|---|
| STD_C | 917 | 417 | 11 |
| A_C | 472 | 83 | 1 |
| A_NC | 306 | 83 | 4 |
| B_C | 250 | 139 | 1 |
| B_NC | 111 | 56 | 1 |

Table 20: Density of bubbles in BF layer below tomography detection limit and number of bubble lines for the used crucible samples. Average value of two series.

| Used crucible | Total density $[cm^{-3}]$ | Border region density $[cm^{-3}]$ | Bubble lines |
|---|---|---|---|
| STD_C | - | - | - |
| A_C | 56 | - | 0 |
| A_NC | 56 | - | 1 |
| B_C | 222 | 167 | 4 |
| B_NC | 28 | - | 2 |

Table 21: Density of bubbles in BF layer below tomography detection limit and number of bubble lines for the heat-treated crucible samples.

| Heat treated crucible | Total density $[cm^{-3}]$ | Border region density $[cm^{-3}]$ | Bubble lines |
|---|---|---|---|
| STD_HT1_C | 1333 | 338 | 20 |
| STD_HT2_C | 889 | 338 | 11 |
| STD_HT3_C | 389 | 278 | 2 |
| STD_HTCZ_pos1 | 142 | 80 | 10 |
| STD_HTCZ_pos4 | 942 | 302 | 12 |
| A_HT1_NC | 391 | 249 | 15 |
| A_HT2_NC | 364 | 169 | 5 |
| A_HT3_NC | 611 | 167 | 2 |
| A_HTCZ_pos1 | 142 | 53 | 2 |
| A_HTCZ_pos4 | 169 | 80 | 1 |
| B_HT1_C | 302 | 27 | 0 |
| B_HT1_NC | 302 | 27 | 1 |
| B_HT2_C | 222 | 53 | 0 |
| B_HT2_NC | 418 | 169 | 1 |
| B_HT3_C | 167 | 111 | 0 |
| B_HT3_NC | 0 | 0 | 0 |

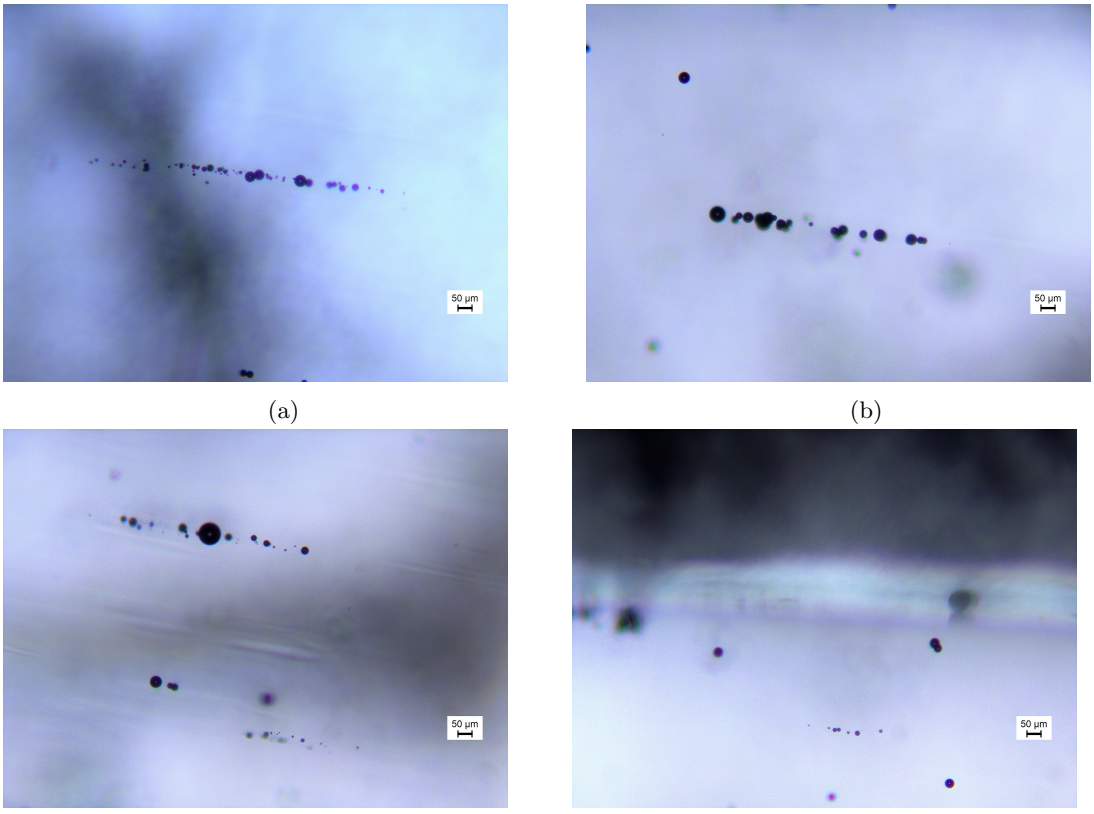


(a) (b) (c) (d)



Figure 41: Transmission microscope pictures of bubble lines in the new STD crucible.

## 4.6 Bubble distribution

Figure 42 shows X-ray tomography cross-sections of the new crucible samples where all the bubbles of each 1 $cm^3$ sample are projected onto one slice. The coloring. is linked to the size distribution. The smaller the bubble volume the bluer the color. The larger the volume, the more the color is shifted towards the red part of the spectrum. Figure 43 shows the corresponding information for the used crucible samples. Figure 44 and 45 show how the size distribution changes from Position 1 to Position 4 in the Czochralski heat treated crucible samples of STD and A, respectively.

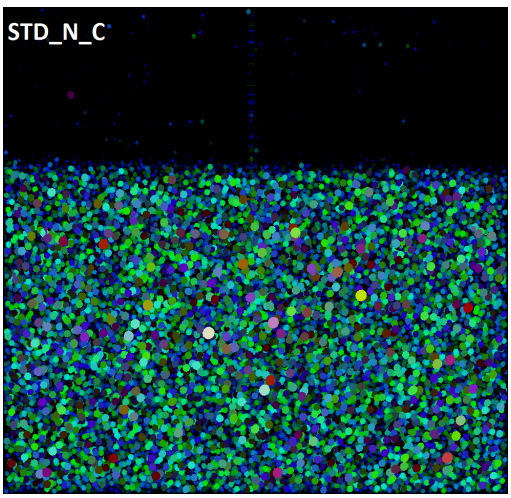


(a)

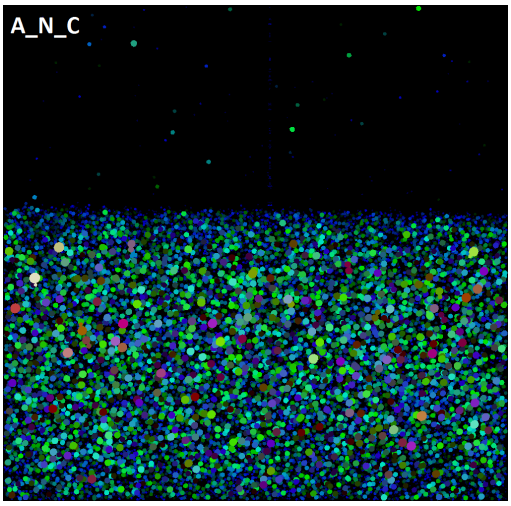


(b)

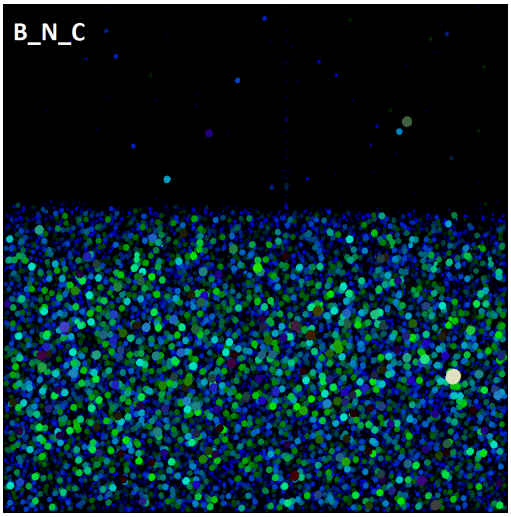


(c)

Figure 42: Tomography cross-sections of the new crucibles samples of STD (a), A (b) and B (c). All bubbles in the 1 $cm^3$ samples are projected onto one slice.

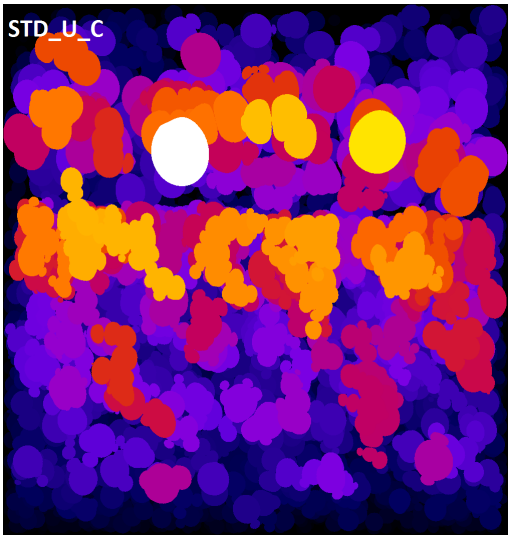


(a)

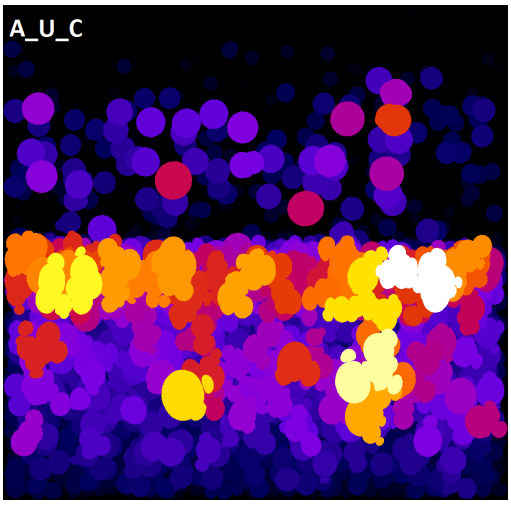


(b)

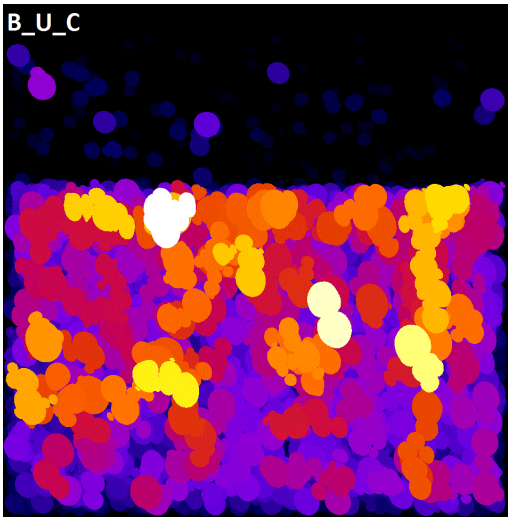


(c)

Figure 43: Tomography cross-sections of the used crucibles samples of STD (a), A (b) and B (c). All bubbles in the 1 $cm^3$ samples are projected onto one slice.

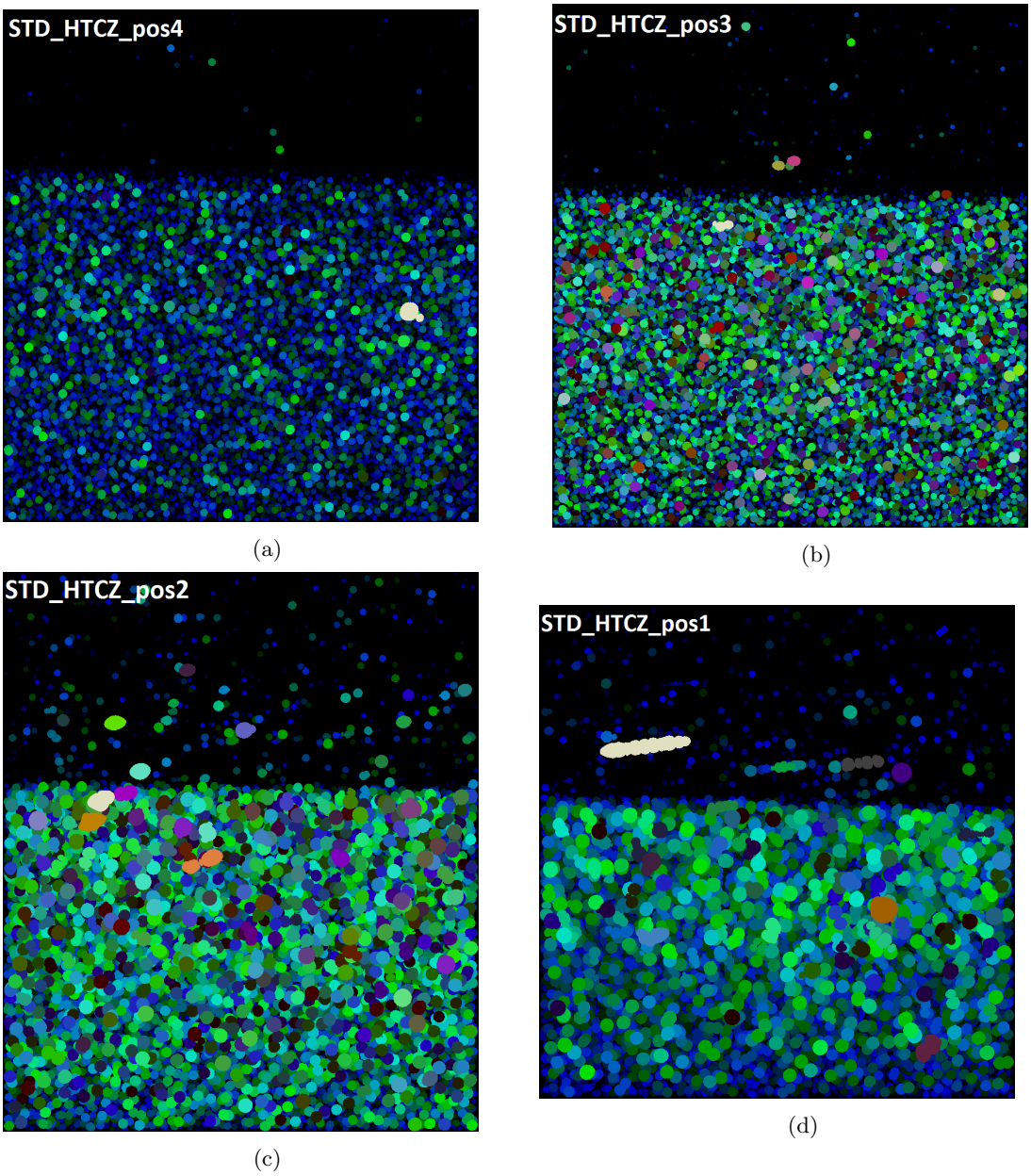


Figure 44: Tomography cross-sections of the STD crucible samples heat treated in the Czochralski puller for Position 4 (a), Position 3 (b), Position 2 (c) and Position 1 (d). All bubbles in the 1 $cm^3$ sample are projected onto one slice.

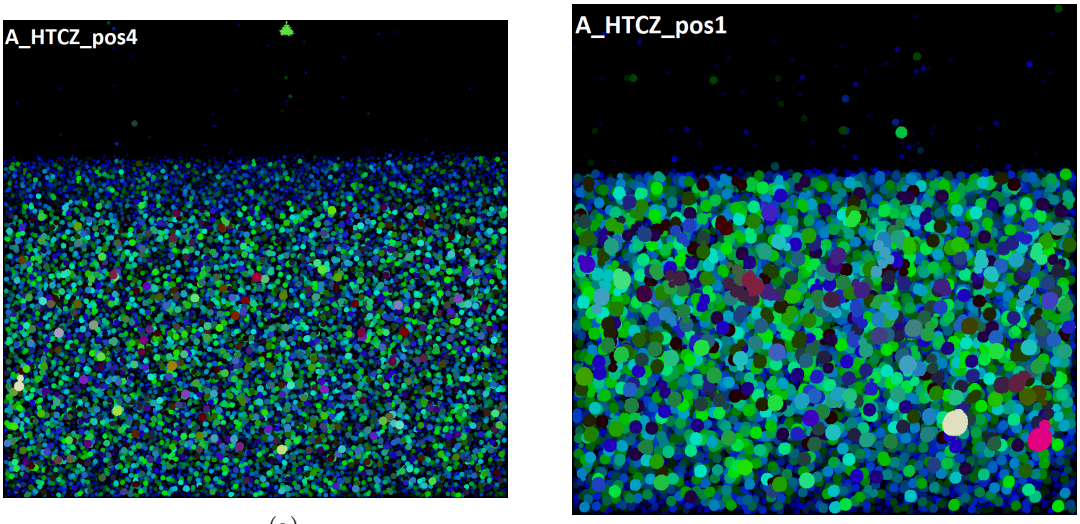


(a) (b)

Figure 45: Tomography cross-sections of the A crucible samples heat treated in the Czochralski puller for Position 4 (a) and Position 1 (d). All bubbles in the 1 $cm^3$ sample are projected onto one slice.

## 4.7 Trace elements

Figure 46 to 48 show the impurity levels of different trace elements in the crucibles under investigation. The measurements are done through the use of inductively coupled plasma mass spectrometry (ICP-MS) and are provided by the Quartz Corp[41].

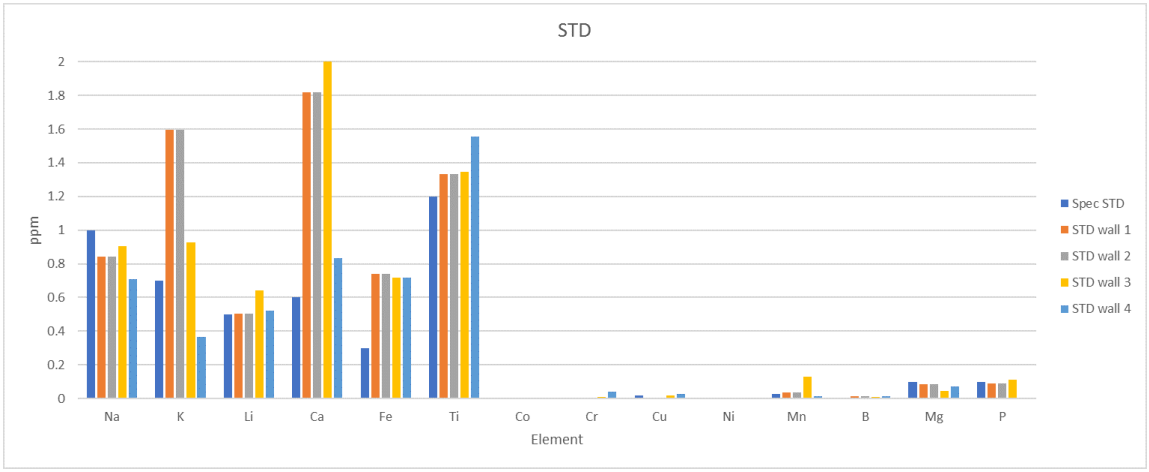


Figure 46: Plot of impurity levels in ppm versus impurity type for crucible STD as measured by ICP-MS[41].

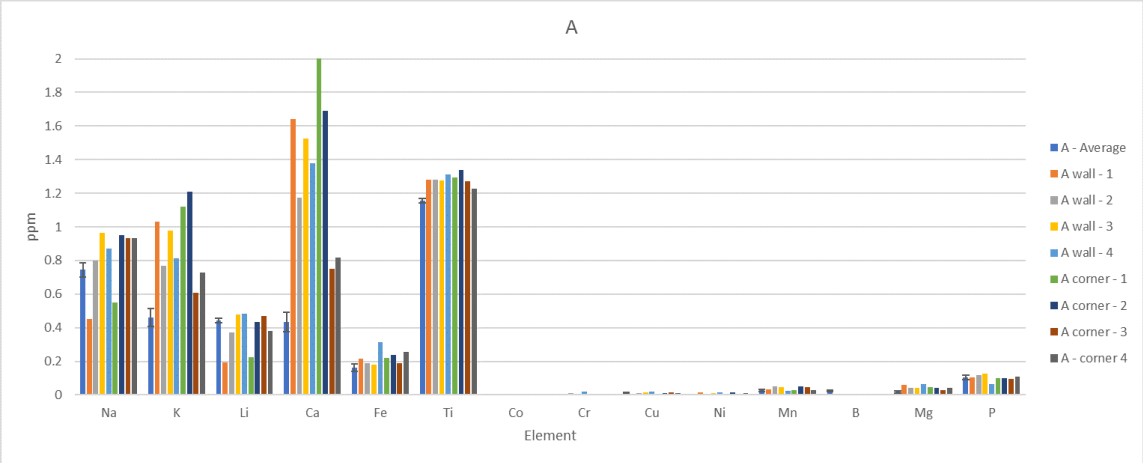


Figure 47: Plot of impurity levels in ppm versus impurity type for crucible A as measured by ICP-MS[41].

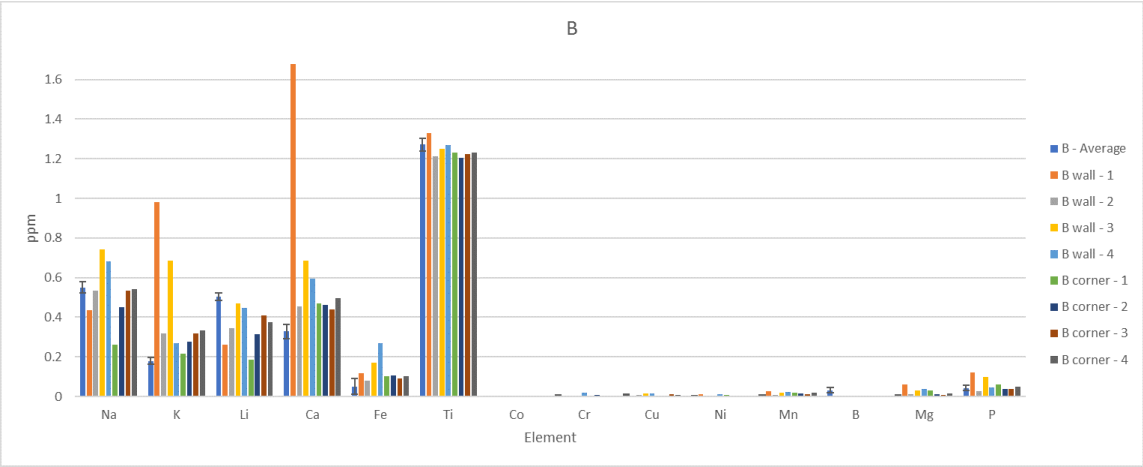


Figure 48: Plot of impurity levels in ppm versus impurity type for crucible B as measured by ICP-MS[41].

# 5 Discussion

## 5.1 Heat treatments

### 5.1.1 Concerns related to testing and silicon melting

The container crucibles that were heat treated in the Muffle furnace in Test 1 were both cracked open and had experienced extensive formation of cristobalite. The silicon feedstock had melted in both containers, but no silicon had spilled out. This indicates that the cracking of the containers happened during the cool-down phase when the silicon had already solidified. The quartz rod in the coarser feedstock had been pressed upwards due to the buoyancy in the silicon melt. One disadvantage with the Muffle furnace compared to the VGF furnace is that the samples are exposed to oxygen. This may promote the cristobalite formation. Furthermore, in the Muffle furnace the container crucibles have no support of graphite elements and the heating is non-homogeneous due to the heating elements being positioned on one side only in the furnace chamber. As the second test was performed in the VGF furnace, the samples had the advantage of being heated uniformly in an inert Argon atmosphere. However, although the temperature was supposed to be above the melting temperature of silicon, the silicon had not melted in any of the two container crucibles and there were no signs of cristobalite formation. There were, however, signs of melting in the top layer of one of the crucibles. This could be explained by too extensive loss of heat through the graphite isolation elements towards the sides of the furnace. Furthermore, only two of four sample compartments in the sample holder were filled which could cause a non-homogeneous heat distribution and explain why the silicon did not melt. Because of this, samples were placed in all four sample holders before Test 3. In addition, the holding (dwell) time and temperature were slightly increased. This resulted in melting of the silicon in all four crucible containers.

### 5.1.2 Crack formation

Both sample A_NC_melt and B_NC_melt experienced considerable crack formation during the 1.5 hour heat treatment. As can be seen in Figure 49, crack formation is a problem because the cracks have the same brightness level as the bubbles in the X-ray tomography pictures. The cracks are thus accounted for as bubbles in ImageJ which gives an overestimation of the bubble content. The crack formation is most likely to happen during the cool-down of the samples as the temperature dependent phase transformation causes the quartz structure to change and thus induces stress in the material. It is, however, only samples exposed to the silicon melt that experienced extensive crack formation. The silicon melt has larger heat capacity than the surrounding argon atmosphere and should cool off more slowly. However, the crack formation may also have been initiated by stress inflicted to the material prior to heat treatment. This could have happened during the sawing of the quartz rods. However, crack formation was only a minor problem as only four out of 30 heat treated samples could not be analysed due to crack formation. Some of the samples outside the silicon melt did also experience minor crack formation. However, this only resulted in a slightly smaller sample volume that could be analysed.

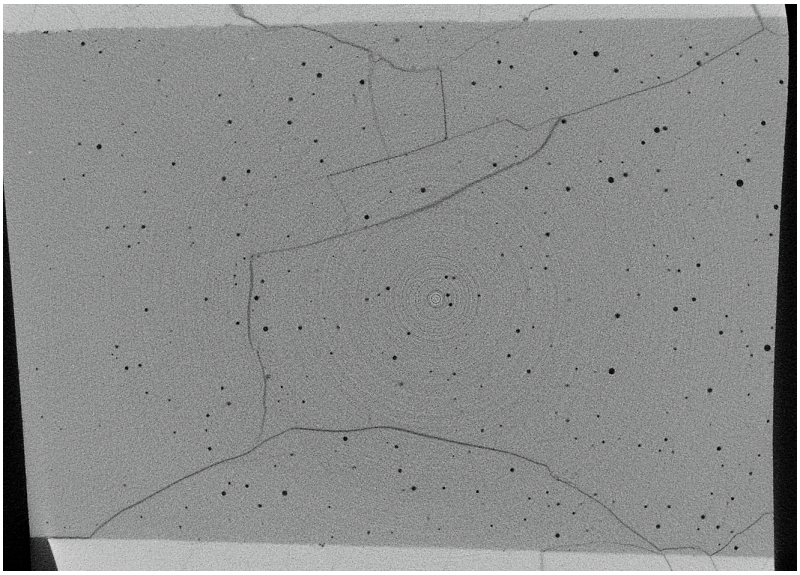

Figure 49: X-ray tomography cross-section showing crack formation in a heat treated crucible sample.

## 5.2 Bubble percent

### 5.2.1 New and used crucibles

It can be seen from Figure 24 and 25 that there is a large difference between the bubble content in the new crucibles and the crucibles heat treated on an industrial scale. None of the new crucibles have a bubble content exceeding 1 % whereas e.g. STD_C used and B_NC used reach a bubble percent of 45 % at the highest. Both for the new and used crucibles there is a distinct border between the BC and BF layer, where for the new crucibles the bubble percent drops to almost zero in the BF layer. It is not evident from the graphs in Figure 24 that there are big differences in the bubble content of the BF layer between the new crucibles of different type. The differences are more obvious for the BC layer, where STD_C seems to have the largest bubble content. Furthermore, STD_C has, as the only new crucible sample, a peak close to the BC-BF border. This type of peak is more distinct in the plots for the used crucibles in Figure 25. At the beginning of the BC layer the bubble content is relatively low, but then it increases almost linearly before a sudden increase right in front the BC-BF layer border before it decreases to values close to zero. The origin of this peak-type and the linear increase was discussed in my Project work[4], but a short repetition will be given here. The linear increase can be explained due to the vacuuming during crucible fusion. For the outer crucible layer (BC layer) the vacuum strength is much lower than for the inner crucible layer (BF layer). Thus, the finished crucible has more bubbles towards the inner part of the crucible. This is more evident for the used crucibles where the bubbles have had time to expand. The border peaks can be explained by the principle of minimization of free surface energy. Large bubbles have a smaller surface to volume ratio and are energetically more favourable than small bubbles[38]. At the BC-BF border the larger bubbles grow at the expense of the smaller bubbles and the growth may be further enhanced by the dissolution of smaller bubbles in the BF layer. Furthermore, as

will be discussed in Section 5.6 about bubble distribution, the bubbles at the BC-BF border tend to grow into each other and form large clusters. This explains the secondary maximums, or depletion regions, that can be seen in the BF layer for all the crucible types, with the exception of A_NC and B_C in Figure 25. Both crucible A_NC and B_C have peaks at the border that are small compared to the other samples, which may imply that there were not as high content of bubbles in the BF layer of these crucibles that could dissolve to support the growth of the border peaks.

An interesting observation is that the depletion regions in the BF layer of the used crucibles in Figure 25 are not easily predicted from the bubble content in the BF layer of the corresponding new crucibles in Figure 24. It has to be taken into consideration that the detection limit of the X-ray tomography scanner is equivalent to the size of one voxel, which is a cube with edges of approximately 9 $\mu m$. Thus, bubbles with diameter below 9 $\mu m$ are not detected. There are indeed more bubbles in the BF layer than what can be seen from the plots in Figure 24. This has been shown through the use of transmission light microscopy and will be further discussed in Section 5.5. However, it must also be taken into consideration that the new and used crucible of the same sand type investigated here are different crucibles. The content of bubbles is not only dependent on the sand quality, but also on manually controlled processes druing and after crucible production. E.g. during crucible fusion the vacuuming is controlled manually. Therefore, if there is a delay in the process and the melting front stops for a moment, typically what happens is that bubbles start to form in lines along the melt border. As will be discussed later in Section 5.5 this is what has happened with the STD_C sample and which probably explains its large secondary maximum. Other human related sources of variation is the pouring of quartz sand into the graphite mold before crucible fusion and the stacking of silicon into the crucible before crystal pulling. The differences between the crucibles of the same type become more evident when comparing the results in this work with the results from my Project work where the same crucible types have been investigated[4].

As already mentioned, the used crucible of STD_C has a large content of bubbles in its BF layer with a maximum reaching almost 25 % bubbles per area. However, also A_C and B_NC have distinct secondary maximums in their BF layer. The differences in bubble content are more obvious when considering the bubble volume percent for the different crucible layers. As can be seen in Table 7, the BF layer bubble content for STD_C is 14.3 % whereas the other samples with secondary maximums, A_C and B_NC, have a BF layer bubble percent of 1.94 % and 1.72 %, respectively. The bubble content in the STD crucible is far beyond what would normally be expected in a fused quartz crucible of this quality. As can be seen in Table 6, the new crucible of STD_C has a BF layer bubble content which is about twice that of the others. However, the difference is smaller for the new than for the used crucibles.

In the introduction a hypothesis was stated that the cristobalite layer may act as a heat shield and thus reduce the bubble expansion in the outer part of the BF layer. This means that a coated crucible should experience less bubble expansion in this part of the BF layer as the coating promotes the cristobalite formation. Of course, for the new samples the coating has no effect as the cristobalite layer only starts to form at temperatures above 1000 °C. This is confirmed by the results in Table 6, where both crucible A and B have rather similar bubble contents in all their respective layers when comparing their coated and non-coated version. The similarities with respect to bubble content show that for these crucibles the fusion process and the other manually controlled processes have been handled properly. The control of the crystal seed dipping into the silicon melt and the

starting point for ingot pulling are determined manually. There may be hours of difference between how long a crucible has to contain the silicon melt. The holding or dwell time is here referring to how long each crucible was in contact with the silicon melt. Crucible A_NC had a holding time of only 37 hours compared to a holding time of around 100 hours for crucible A_C. This explains why the non-coated crucible A has a lower bubble content than its coated counterpart. The remaining used crucibles all had holding times of around 100 hours. From Table 7 it can be seen that the non-coated crucible B has a total bubble content and BC layer bubble content almost similar to that of the coated crucible B. However, the bubble content in the BF layer is three times larger in the non-coated crucible. Furthermore, the holding time of the two crucibles is about the same. H. Hendrickx did investigation on the cristobalite layer thickness for the two B samples in a parallel work. Her results show that B_C has a cristobalite layer thickness of about 270 $\mu m$ whereas B_NC has a thickness of about 50 $\mu m$[37]. This indicates that, for crucible B, the cristobalite layer could have had a restricting effect on the bubble formation in the outer part of the BF layer. However, no conclusion can be drawn on one result only. The variation in bubble content from crucible to crucible may be considerable. As will be discussed in the next section, the results for the heat treated samples in Table 8 to 11 do also show a possible trend with the coated crucibles having a slightly lower bubble content than the non-coated.

### 5.2.2 Heat treated crucibles

From Figure 26 to 28 it is evident that the general bubble content increases with temperature and holding time when comparing the heat treated samples with the new samples in Figure 24. All the heat treated samples experience an increase in total bubble content. The longer the samples are heat treated the higher their bubble volume becomes, at least up to a certain point. Table 8 to 11 give information about the bubble volume percent in the different parts of the crucible for the heat treated samples. The samples that lack data about bubble percent have experienced extensive crack formation during the heating which made it impossible to distinguish the bubbles from the cracks. When looking at the bubble content for the whole sample, it can be seen that the coated B samples on average have a slightly lower bubble content than their non-coated counterparts. However, when looking at the BF layer alone, the results are not consistent. E.g. B_NC_top has a lower BF layer bubble content than B_C_top for the 1.5 h experiment. The same is the case for B_NC_melt compared to B_C_melt for the 10 h experiment. However, both for the 1.5 h and 10 h experiment the difference in thickness of the cristobalite layer between coated and non-coated samples is less than 10 $\mu m$[37]. For the 24 h experiment the thickness difference is larger as B_C_top has a cristobalite layer about 80 $\mu m$ thicker than that of B_NC_top. However, the BF layer bubble content of B_NC_top is the lowest measured. This is explained by the fact that sample B_NC is a corner sample due to lack of wall material. Corner samples tend to have a thinner BF layer and a lower content of bubbles than wall samples[26]. This, however, makes it difficult to compare it with the B_C 24 h sample as this is from a wall position. When looking at the results for sample A in Table 8 and 9, it can be seen that there is hardly any difference between A_C and A_NC for the 1.5 h and 10 h experiment. In fact, the BF layer bubble content has hardly increased in either of these samples compared to the initial bubble content in the new samples in Table 6. The only real increase in BF layer bubble content is observed for A_NC_melt in Table 9 and A_NC_top for the 24 h experiment in Table 10.

A general trend which becomes more evident with increased holding time is that crucible STD

on average has the highest bubble content. As seen in Table 9 for the 10 h experiment, the BF layer bubble content of the STD samples is about twice the bubble content of B_NC_top which has the third largest BF layer bubble content after the STD samples. The exception is for the 24 h experiment in Table 10 where A_NC_top has the highest BF layer bubble volume. What is interesting to observe is that the BF layer bubble volume of STD_C_top in Table 9 is 5.7 times higher in the 10 h experiment compared to the 24 h experiment in Table 10. Furthermore, when comparing with the new STD sample in Table 6, sample STD_C_top 24 h has a slightly lower bubble content than its non-treated counterpart. In other words, the BF layer bubble content of STD_C_top does not seem to have increased at all during the 24 hour long experiment. The same is the case for B_C_top 24 h which hardly experiences any change in its BF layer bubble content. It becomes clearer when looking at the increase in percent from one heat treatment to the other. In average for all crucible samples, the total bubble content increases with about 46 % from the new to the 1.5 h heat treated samples, i.e. an increase of around 31 %/h. From the 1.5 h to 10 h samples the average increase is 47 %, or 5.5 %/h. From the 10 h to the 24 h experiment the average increase in total bubble content is only 2.5 %, or 0.2 %/h. In this calculation the corner samples were not included. For the BF layer alone the corresponding increase is 69 % 57 % and 240 % for the new-1.5h, 1.5h-10h and 10h-24h experiment, respectively. Although the increase is large considering the BF layer from the 10 h to 24 h samples, this only applies for two of the samples. The other 24 h samples hardly experience any change in their BF layer bubble content. In other words, there is a large variation from sample to sample. Furthermore, most of the bubble expansion in the VGF heat treated samples seems to take place early in the process, e.g. during the melting phase when the temperature reaches its peak value.

When comparing the difference in bubble content between the sample parts immersed in the silicon melt and the sample parts outside the melt, for the experiments performed in the VGF furnace, it does not seem to be relevant whether the sample is exposed to the melt or not. As seen in Table 8 to 10, it varies from sample to sample whether it is the melt covered part or the part outside the melt that have the highest bubble content. E.g. the bubble content in the BF layer of crucible STD heat treated for 1.5 hour is twice as large in the top part compared to the melt part. However, for crucible B_C from the same experiment the BF layer bubble content is more than four times higher in the melt part. For the 24 h experiment in Table 10 the two melt samples that are analysed have a higher bubble content than the corresponding top samples. However, two of the melt samples are not accounted for due to crack formation. The lack of consistency indicates that the temperature in the VGF furnace has been quite homogeneous. Thus, the local variations within the quartz samples seem to have been the determining factors for the bubble formation and growth. It is important to take into consideration that when the samples were cut, the sample direction was not being accounted for. I.e. it is not known which side of the sample rods that originally came from the top of the crucible and which side that pointed downwards. As briefly discussed in the theory section, the bubble content tends to vary with the lateral position in the crucible. E.g. the corner positions seem on average to have a lower bubble content than the wall positions[26]. However, the rods in these experiments are all taken from the wall position and there are only 5 *cm* separating the top from the bottom position. The bubble content is not expected to vary much at this distance, but it should be kept in mind as a possible influencing factor.

### 5.2.3 Crucible samples from Czochralski experiment

The samples heat treated in the Czochralski puller do not follow the same trends with respect to bubble growth as the samples heat treated in the VGF furnace. The bubble content in the samples immersed in the silicon melt increased several times more in the Czochralski experiment compared to the VGF experiments. As can be seen in Figure 26, the bottom sample (Position 1) of STD_HTCZ_C reaches a maximum BC layer bubble content of more than 9 %. This is about 4.5 times higher than the maximum BC layer bubble content in the corresponding 10 h experiment (HT2) performed in the VGF furnace. However, it is also a larger increase per hour than what is observed for the industrially used crucibles in Table 7. Keep in mind that the holding time of these crucibles is about 10 times that of the Czochralski experiment. The details regarding the bubble volume percent are found in Table 11. It can be seen that the part of the STD rod that was deepest into the silicon melt, i.e. Position 1 in Figure 22, on average has a bubble content of 4.1 %, whereas the corresponding A rod has a bubble content of 2.9 %. This is about 4 times more than the corresponding 10 h samples heat treated in the VGF furnace (although it should be considered that sample A in the VGF experiment is non-coated). When it comes to the BF layer alone, the differences are even larger. The bubble content is approximately 51 times higher and 3 times higher for the STD sample and A sample for the Czochralski experiment compared to the 10 h VGF experiment, respectively. This implies that although the temperature and holding time were intended to be about the same for the two 10 h experiments, the real conditions in the two furnaces have deviated to a large degree. Firstly, the temperature in the Czochralski puller is measured with a pyrometer above the surface. I.e. one cannot be completely sure that the temperature inside the melt is exactly as expected. Secondly, the sample rods experience a greater thermal shock when being lowered into the already melted silicon in the Czochralski furnace compared to a gradual temperature increase while the silicon melts in the VGF furnace. In the Czochralski melt there is more motion due to rotation of the crucible and a different heat flow due to the argon gas flow from above. The Czochralski experiment is probably closer to the real situation as the set-up is closer to the industrialized process. However, the bubble growth in the Czochralski experiment was higher than for the industrial case. This strengthens the assumption that most of the bubble expansion happens early in the process.

While the bubble content in the sample exposed to the silicon melt and the sample outside the melt does not differ to a large degree for the VGF experiments, there is a large difference between the exposed and unexposed samples from the Czochralski experiment. As can be seen in Table 11, for crucible STD the average bubble content decreases from 4.1 % to 3.9 % from the part of the rod deepest into the melt (Position 1) to the part directly below the melt surface (Position 2). However, directly above the melt surface the bubble content reduces to about 1 % (Position 3) and then continues to reduce to 0.57 % in the top part (Position 4). It should be kept in mind that the samples are taken from four positions directly next to each other. The bubble content in the top position for the HTCZ samples is about the same as the samples heat treated 1.5 hour in the VGF furnace. The results indicate that there are large variations in the conditions above and below the melt in the Czochralski puller. The results from the temperature simulations in Figure 29 and 30 show that this is indeed the case. As seen in Figure 29 the temperature varies with approximately 370 °C from the top to bottom position of the crucible rods. As also seen in Figure 30 the temperature drop in the quartz rod is most significant across the melt border. In the area around the quartz rod the temperature is lower than everywhere else in the area close to the melt. Fused quartz is a good insulator. However, it is still a surprise that the temperature is not more

homogeneous during the 10 hour long experiment.

The lower temperature in the upper part of the quartz rod is probably best explained due to the cooling effect of the argon gas flow. Argon gas is flowing down the heat shield and follows the side of the crucible wall. When it hits the melt surface, the gas is pushed towards the center part of the melt. Because the silicon melt is in motion due to the crucible rotation and internal heat flux, the argon gas will not be able to cool the dynamic silicon surface. However, the stationary quartz rod is more easily cooled. Furthermore, there are some limitations with the simulation compared to the real experiment. The simulation only accounts for one quartz rod whereas the real experiment had six. Only the four cm at the bottom of the rod are accounted for. In the real experiment, the argon gas flow will be slightly different around the six rods and follow the whole length of the rods. The thermal conductivity of quartz is quite temperature dependent. The simulation uses a fixed value of 4 $W/Km$. A simulation was also run with a fixed thermal conductivity of 7 $W/Km$, but the results were almost the same.

For the samples heat treated in the Czochralski puller the STD crucible has a bubble content larger than that of crucible A, i.e. the same trend as for the experiments performed in the VGF furnace and the industrially used samples. The difference is larger for the sample parts in the silicon melt. For Position 1 (bottom) STD has a BF layer bubble content 11.6 times higher than that of the corresponding position in sample A. However, when looking at the graph for the bottom position of STD in Figure 26, it can be seen that the large BF layer bubble content is mainly caused by two secondary peaks close to the BC-BF border. It is unlikely that these bubbles will reach the silicon melt as they are far away from the crucible-melt interface. As already mentioned, the results here are only based on two crucibles for each crucible type, one new and one used (all heat treated samples are prepared from the new crucible). The crucibles in this work are from a batch were 48 crucibles were produced for each type. The crucibles studied in my previous Project work came from another batch where five crucibles were produced per type[4]. By comparing the crucibles of the same type, but from different batches, a more complete picture will be drawn with respect to the bubble content of the different crucible types.

### 5.2.4 Comparison with results in project work

Table 12 gives the bubble percent for new and industrially used crucibles investigated in my Project work[4]. By comparing these results with the results from Table 6 and 7 in this work, it can be seen whether the crucibles have been reproduced with high accuracy with respect to bubble content. It becomes evident when comparing the tables that both crucible A and crucible B from the Project work have bubble contents in both layers that match well with the corresponding crucibles in the Master work. This indicates that the quartz sand maintains high quality and that the crucible fusion and other manually controlled processing steps have been controlled properly for the crucibles in both batches. However, there is one exception. The STD_C used crucible in this work has a total bubble content of 22.7 % and a BF layer bubble content of 14.3 %. The corresponding bubble contents in the STD crucible from the Project work are 13.2 % and 0.37 %. In other words, the BF layer bubble content is 38 times higher in the STD crucible studied in this work. As can be seen in Table 12, STD used in the project work has the lowest BF layer bubble content of the three crucibles studied, i.e. the opposite of the results from this work. An external test was run on the STD crucible in this work, using inductively coupled plasma mass spectrometry (ICP-MS), to

see if the high bubble content could be related to a higher impurity content in the form of metals and alkali elements. It can be seen from Figure 46 to 48 that all crucibles have elevated levels of calcium (Ca)[41]. The levels of titanium (Ti) and potassium (K) are also rather high. Crucible B has, on average, a lower level of Ca and K than STD and A. The similarities in impurity content between STD and A, and partly also B, indicate that these impurities have been incorporated in the crucibles during crucible manufacturing. In other words, this is most probably a fusion related problem and not related to the sand quality. To sum it up, crucible A and B have approximately the same bubble content in both the BC and BF layer for the crucible samples from both batches. The STD crucibles, on the other hand, deviate to a large degree with respect to bubble content. In Section 5.5, where the number of bubble lines in each sample is counted, more arguments will be given why this most probably is related to the crucible fusion. The new STD crucible in this work has an average bubble content about 1.2 times higher than the new STD crucible in the project work. Even though this is a less significant difference compared to that of the used crucibles, there may be a high amount of bubbles below the detection limit. This is discussed in Section 5.5.

When taking into consideration all the above results, it will here be given a temporary conclusion on which crucible type that shows the most promise with respect to low expansion and content of bubbles in the BF layer. STD is the crucible with the highest degree of variation between the crucible batches and also the highest bubble content by far for the sample studied in this work. Both the new and used STD samples have on average a BF layer bubble content several times higher than the A and B crucible. When it comes to the differences between crucible A and B, they both have a rather similar BF layer bubble content for their new crucibles. The used crucible A_C, on the other hand, has a BF layer bubble content 3.5 times higher than B_C. The differences are not that evident for the heat treated samples and varies considerably with sample position. When that is said, only one crucible of each type were tested per batch. Therefore, the statistics are too low to draw any finite conclusion. When it comes to the uncertainty in the X-ray tomography measurements, the deviation within a crucible is larger than the deviation between one measurement and the next.

## 5.3 OH content

Table 13 to 18 give the OH content in parts per million (ppm) for all crucible samples, both new, used and heat treated. As already explained in the theory section, a high OH content lowers the viscosity of the quartz and thus makes it easier for bubbles to expand. Therefore, one could think that a high bubble content in a heat treated sample would correlate with a high OH content. However, another factor must also be taken into consideration. Namely, that hydrogen tends to diffuse in the quartz and form bubbles at elevated temperature. This is used deliberately during crucible production to decrease the OH content[41]. However, as some OH groups remain in the quartz structure, these are likely to diffuse during crystal pulling. The idea is, therefore, that one should observe a correlation between a reduction in OH content and an increase in bubble content with increased holding time.

Figure 31 shows a plot of the OH content in ppm along the y-axis versus the different heat treatments along the x-axis. It can be seen from this plot that there is a reduction in OH content from the new to used crucibles. The reduction is most evident for crucible A, where the OH content is 167 and 92 ppm for the BC and BF layer of the new sample, respectively. In the used crucible A

the OH content is only 31 ppm in the BF layer. This reduction of 61 ppm OH implies that there has been rather high diffusion of hydrogen. Other evident examples of OH reduction in the BF layer is from STD_wall new (64 ppm) to STD_wall used (20 ppm), a reduction of 44 ppm. Another is the reduction of 33 or 20 ppm, from B_wall new to B_wall used, depending on which part of the sample that is considered. STD_corner, on the other hand, has a reduction of only 4 ppm from the new to used crucible. Keep in mind that the new and industrially used crucible of the same sand type is not the same crucible. The local content of OH groups varies a lot through the crucible samples. Therefore, some of the OH measurements are given by two different values. If the difference between the two measured positions exceeds 10 ppm, both values are given instead of the average value. It is interesting to observe that the decreasing order of OH content in the used crucibles correlates with the increasing order of bubble content. STD_wall used, which has the lowest OH content of the used crucibles, has the highest BF layer bubble content as seen in Figure 25. A_wall used which has the second lowest OH content has the second highest bubble content.

The heat treated crucible samples are taken from the new crucibles studied in this work and the relation in OH content between the new and heat treated samples can, therefore, be directly compared. The difference in OH content is not that evident for the crucibles heat treated in the VGF furnace. Remember, however, that the holding time is shorter for these samples compared to the industrially heat treated (used) samples. Thus, for the 1.5 h to 24 h heat treatments there was less time for the diffusion to take place. It can be seen, when comparing the new samples with the 1.5 h heat treated samples in Figure 31 and Table 13 and 15, that their OH content is quite similar. The samples have an average OH level of 79 ppm and 75 ppm, respectively. At the same time, the bubble content experiences an average increase of 46 % from the new to 1.5 h heat treated samples. The samples heat treated for 10 hours have experienced, on average, a reduction in OH content of about 15 ppm compared to the 1.5 hour samples, which is a considerable change (This calculation only considers the lowest measured OH value in the samples). The bubble content, on the other hand, has increased with 47% from the 1.5 h to 10 h samples. However, when comparing the 10 h samples with the 24 h samples it can be seen that the OH content has not changed much. As can be seen in Table 17, almost all B samples heat treated for 24 hours have a higher OH content than the corresponding B samples heat treated for 10 hours. On average the OH content is 3 ppm higher for the 24 h samples compared to the 10 h samples. This may be a surprise as the hydrogen have had 14 hours more to diffuse. However, the total bubble increase from the 10 h to 24 h samples is only 2.5 %. This gives a rather good indication that the reduction in OH content correlates with the bubble growth. Nevertheless, crucible STD and B do not experience the same reduction in OH content with increased holding time as A. This shows that the local variation in OH content may be considerable. Two positions in the same crucible sample at a distance 5 $mm$ apart may have a difference in OH content of as much as 10 ppm.

Of the heat treated crucible samples, it is those heat treated in the Czochralski puller that show the largest reduction in OH content. The results for the Czochralski samples are not accounted for in Figure 31, only Table 18. Keep in mind that the sample rods have experienced a temperature difference of 370 °C between the top (Position 4) and bottom (Position 1) position. Therefore, the bottom position in the highest temperature region should have experienced more diffusive motion and thus a lower OH content. Table 18 confirms this. For STD_BF_top to STD_BF_bottom the OH content difference is 27 or 15 ppm depending on which position that is considered. The corresponding bubble content is 42 times higher in the bottom position compared to the top position.

Sample A has a similar difference of 10 ppm between the top and bottom position for its BF layer and a difference of 40 ppm for its BC layer. The corresponding bubble content is 6.7 times higher in the bottom position for the BF layer of A and 6 times higher in the bottom position for the BC layer. This means that although the BC layer of A experienced the largest difference in OH content, it did not experience the largest difference in bubble content. In other words, it is difficult, from these results, to predict the increase in bubble content based on the decrease in OH content. The local variation in OH content is simply too large. However, the above results do indicate that the OH content may be an important parameter to consider when explaining the reasons behind large bubble expansion. Keep in mind that the bubble growth is also caused by gas expansion and not hydrogen diffusion alone.

## 5.4 Crucible cross-sections

As seen in Figure 32c and d, the bubble content of the cross-sections of STD_U correlates well with the STD plot in Figure 25. There are large bubbles in the BF layer of both sample series. In Figure 32c the bubbles are even positioned directly at the crucible-melt interface. However, as already emphasized, this does not necessarily mean that this is a typical trend for the STD crucible. When comparing the used crucibles with the new ones in Figure 32a and b it is obvious that the new crucibles do not have any bubbles in their BF layer, at least not in the sample sections that are visible in the pictures. However, as discussed in Section 5.5 there are indeed more of the bubbles below the detection limit in the STD crucible compared to the others. Considering that the bubbles below detection limit are the origin of the large bubbles in the BF layer of STD_U, this would imply a large bubble expansion. For the STD crucible, where the bubble diameter in a used crucible on average is approximatley 300 $\mu m$[4], this corresponds to a volume increase of about 27 000 times.

As already discussed, A_U_C has a higher bubble content in its BF layer and in the crucible sample in general compared to A_U_NC due to its longer holding time. It can be seen from the cross-sections in Figure 33c and d and Figure 34c and d that the bubbles of A_U_NC on average seem to be smaller than those of A_U_C. In other words, this confirms the higher bubble content in the coated crucible. As seen in Table 7, crucible B_U does not differ much in total bubble content between the coated and non-coated crucible. However, the BF layer bubble content is higher in the non-coated crucible. This is to a certain degree also confirmed in the cross-sections in Figure 36c and d, which both have larger bubbles in the BF layer while the coated version in Figure 35c and d does not.

The bubbles in the cross-sections of the heat treated crucible samples seem to have increased in size compared to those of the new samples. This can e.g. be seen for the 1.5 h heat treated STD sample in Figure 37a and the 10 h heat treated STD sample in Figure 38a. However, no bubbles in the BF layer can be seen in any of these cross-sections. The same is the case for the heat treated crucible samples A and B. Be aware that the features in the BF layer of Figure 38a are surface defects and not bubbles. The bubbles have increased in size, but the number of bubbles seem to be about the same. Not even the STD samples heat treated in the Czochralski puller have any considerable BF layer bubble formation, although some small bubbles can be seen in Figure 40a. There are differences, however, between the top parts and the parts that were in contact with the silicon melt. As seen in Table 11 for crucible STD, the bubble content is about 7 times higher in the sample that was in contact with the silicon melt. It can be seen from Figure 40a and b that the

bubbles are indeed larger in the melt sample. Not only the bubble volume, but also the number of bubbles is higher in STD_melt compared to STD_top. The total number of bubbles in the BC layer of the melt sample in Figure 40a is 82 whereas the number is 52 for the top sample in Figure 40b. For crucible A heat treated in the Czochralski puller, the melt sample has a total bubble volume about 5.5x larger than that of the top part and the number of bubbles in the cross-section is 76 and 54 for the melt and top part, respectively. It is also interesting to observe that the average bubble size has hardly increased from the 10 h to the 24 h experiment. This confirms the results from the tomography scans as the calculated increase in total bubble volume only is 2.5 % from the 10 h to 24 h samples. When it comes to the uncertainty in the measurements, the same situation applies as for the tomography measurements. The local variation in OH content is even greater than the local variation in bubble content. Thus, the sample variation is far greater than the variation related to uncertainty in the FTIR spectrometer measurements.

## 5.5 Bubbles below tomography detection limit

It can be seen from Table 19 to 21 that all crucible samples, except for B_HT3_NC, contain bubbles with sizes below the X-ray tomography detection limit, i.e. are below 9 $\mu m$ in diameter. Crucible STD stand out as the one with the highest content of these bubbles, with a density between 142-1333 $bubbles/cm^3$ for the new and heat treated samples. It can be seen from the tables that the density of the bubbles below detection limit correlates well with the general bubble content of the crucibles. STD new has a density of the sub-detection limit bubbles which is almost the double of that of A_C new which has the second highest density. This corresponds well with the plots in Figure 25 and may explain why crucible STD has such a large BF layer bubble content. For the used STD samples, the BF layer bubble density is too high for enough light to transmit through the sample. Therefore, the bubble counting becomes difficult. There may thus be more bubbles below the detection limit in the used samples than what is indicated in Table 20. It is only the bubbles near the crucible-melt interface that may have influence on the silicon melt. Crucible STD new has a border region density of 417 $bubbles/cm^3$, and these are only the bubbles below the detection limit. In other words, a high number of bubbles may potentially end up in the silicon melt from this crucible sample during crystal pulling. It should be taken into consideration that the high density of bubbles below the detection limit for the STD crucible to a large degree is due to bubbles part of bubble lines as seen in Figure 41. E.g. as seen in Table 21, sample STD_HT1_C has 20 bubble lines in a volume of 0.4 $cm^3$, i.e. 50 $lines/cm^3$. It can be seen from the tables that a high density of bubbles often correlates with a high number of bubble lines. As already explained in the theory section, bubble lines are created during crucible fusion if the vacuuming is not adjusted for properly during the movement of the melt border. However, the bubble lines more often appear in quartz crucibles made of low-quality quartz sand[15]. Thus, this is a phenomenon resulting from the combination of human influence and quartz sand quality. As can be seen in Figure 41d, where the edge of the crucible is visible, the bubble line is parallel to the crucible-melt interface. This is the case for all the bubble lines found in the samples and is evidence that they form along the melt border during crucible fusion. In this work, bubble lines can be found in crucible samples of all three crucible types. However, as can be seen in Table 19 and 21, they appear more frequently in crucible STD than in A and B, and more often in A than in B.

For crucible A and B the density of bubbles below the tomography detection limit is lower than that of STD and also varying more with sample position. There is no clear evidence that there is a

difference in the bubble density between coated and non-coated samples. The local variation of the samples of the same type in between is larger than the variation between coated and non-coated samples. For the new crucible samples, as can be calculated from Table 19, crucible B has on average a border region density of 98 $bubbles/cm^3$. The corresponding density for A is 53 $bubbles/cm^3$. However, when looking at the samples heat treated in the VGF furnace, crucible A has an average border region density of 195 $bubbles/cm^3$ whereas that of B is 77 $bubbles/cm^3$. The corresponding value for STD is 318 $bubbles/cm^3$. In other words, it seems that crucible B has the lowest density of bubbles below detection limit in the border region when the number of samples investigated increases in addition to temperature and holding time.

When comparing Table 19 and 20, it can be seen that the number of bubbles below the detection limit is reduced after heat treatment. For the used crucibles the sub-detection limit bubble density is only between 28-56 $bubbles/cm^3$. The exception is sample B_C_1 which has more bubble lines than the other samples, whereof three of them are close to the crucible-melt interface. The reduction in number of small bubbles is due to the growth of the bubbles during heat treatment. However, another reason for the reduction may be that the bigger bubbles in the used crucible samples reduce the transmission of light through the sample, thus making it more difficult to detect the smaller bubbles. For the samples heat treated in the VGF furnace the reduction in density is not that evident. As can be seen in Table 21, sample A heat treated for 24 hours (HT3) has a higher density than the corresponding samples heat treated for 10 and 1.5 hours (HT2 and HT1). However, apart from this result the other samples heat treated for 24 hours have the lowest density of the VGF heat treated samples. Furthermore, when looking at the STD_HTCZ sample in Table 21, it can be seen that the bubble content is indeed higher for Position 4 which was subjected to lower temperature than Position 1 inside the melt.

It is important to emphasize that the local variation in bubble density of a sample may vary considerably at distances less than 1 $cm$. As only one crucible has been investigated per sample, the densities here cannot be considered as values typical for the respective crucible types. In addition to this, the method used to count the bubbles is performed manually. The chance of missing out on bubbles when scrolling through the planes of the sample volume is relatively high. Despite of this, as the density of the bubbles below detection limit seem to correlate with the general bubble content of the crucibles, this indicates that they are important for predicting the total bubble expansion from new to used crucibles. Furthermore, if a temporary conclusion is to be drawn from the results here, it is that crucible B on average has the lowest density of bubbles below the detection limit and the lowest number of bubble lines. Crucible STD stand out as the one with the highest density and the highest number of bubble lines. When linking this to the differences in sand quality and chemistry in Table 2, it can be seen that crucible B has a finer particle size distribution than STD and A. As explained in Section 2.2, this implies that more impurities are exposed at the surface of the B quartz sand due to the larger surface to volume ratio. This makes it easier to remove the impurities and implies that crucible B should have a higher quartz sand quality. This could explain why the number of bubble lines and density of bubbles below detection limit are lower for crucible B.

## 5.6 Bubble distribution

The tomography cross-sections in Figure 42 to 45 show the distribution of bubbles in the cubic crucible samples. For the new crucible samples the bubbles are larger the more the bubble color is shifted towards the red part of the color spectrum and smaller the more it is shifted towards the blue part. It can be seen for all the new samples in Figure 42 that their particle size distribution is rather evenly distributed across the BC layer. This is a sign of good vacuum control during crucible fusing and stable movement of the melt border as the bubbles have grown in a controlled manner. Furthermore, the BF layer bubble content is low for all the samples, which corresponds well with the plots in Figure 24. It can be seen from the colors that crucible B seems to have the smallest particle size distribution of the three samples, whereas STD and A contain some larger bubbles as well.

Figure 43a shows that the used STD samples have a high density of bubbles from the beginning of the BF layer and all the way to the crucible-melt interface. This confirms the bubble percent plot of STD in Figure 25, where sample STD has a large secondary maximum in its BF layer. Furthermore, it can be seen that crucible STD contains, on average, larger bubbles in its BF layer than A and B, and there are more of the large bubbles in the BF layer compared to the BC layer. The latter can be explained by the higher viscosity of the BF layer. The BC layer already contains bubbles that stiffen the quartz structure. Thus, it is easier for new bubbles to grow and expand in the BF layer. Sample A in Figure 43b does also have a rather high density of large bubbles in its BF layer. However, not as high as STD and few of them are close to the crucible-melt interface. It is thus unlikely that many of these large bubbles have entered the melt during crystal pulling. Crucible B in Figure 43c has few of the large bubbles in its BF layer and none close to the interface.

Figure 44 shows the bubble distribution in the STD sample heat treated in the Czochralski puller from Position 4 above the melt to Position 1 below the melt (Be aware that the green shape at the top in Figure 45a is a defect and not a cavity). These four pictures illustrate how the average bubble size increases with temperature. Keep in mind that that Position 1 (d) experiences on average a temperature 370 °C higher than the Position 4 (a). It is also evident for crucible STD that the number of visible bubbles in the BF layer increases drastically with increased temperature. However, this is not the case for crucible A. As can be seen in Figure 45, the number of bubbles in the BF layer does not increase that much from the top position (a) to the bottom position (b). However, as can be seen in Table 21, the top sample of crucible STD has a higher content of bubbles below the X-ray tomography detection limit than the top sample of crucible A. This strengthens the assumption that the increased number of bubbles in the BF layer after heat treatment mainly is due to growth of bubbles initially below the detection limit. Impurity inclusions in the quartz acting as nucleation centres could also be a source of the new BF layer bubbles. However, as the impurity content of A and STD is about the same[41], one would expect crucible A to have a higher number of bubbles in the BF layer of Position 1 as well. As this is not the case and because A has a lower density of bubbles below the detection limit than STD, this could explain why the increase is not larger for A and indicates that the difference between the two crucibles is fusion related. Once more it is important to emphasize that there is considerable local variation in the crucible samples with respect to bubble content.

# 6 Conclusion

The results of this work give strong indications that differences in quartz sand quality affect the performance of the crucible through bubble formation and expansion in the BF layer. However, they also indicate that manually controlled processes such as crucible fusion cause great local variation. The bubble content increases considerably when temperature and time are increased. However, the bubble increase seems to be larger in the start phase of the heat treatment. The samples experienced an average increase in bubble content of 46 %, 47 % and 2.5 % for the new-1.5h, 1.5h-10h and 10h-24h heat treatment, respectively. The local variation is large and some of the 24 h heat treated samples did hardly experience any BF layer bubble increase. The bubble content increase is several times higher in the samples from the Czochralski experiment compared to the VGF furnace, however, only for the samples immersed in the silicon melt. The relative bubble increase in the Czochralski samples is also higher than for the industrially used samples. As the Czochralski set-up is closer to the real situation, this strengthens the assumption that most of the bubble growth happens early in the crystal pulling process.

A hypothesis was stated that the crucible coating, and thus cristobalite layer formation, has a restricting effect on the bubble formation in the outermost part of the BF layer. There are results in this work indicating that this may be the case and the coated samples do have a thicker cristobalite layer. However, the statistic is too low to draw any conclusion. Regarding the OH content of the crucibles, there seems to be a correlation between an increase in bubble content and decrease in OH content due to diffusion. This is most evident for crucible A. However, the local variation in a sample is large and it is not possible to predict the bubble increase from the reduction in OH content alone. All crucible types have bubbles below the tomography detection limit in their BF layer. These bubbles seem to be the main source of the BF layer bubble content increase from new to heat treated crucibles. The density of these bubbles seems to correlate with the general bubble content and the number of bubble lines. Both crucible STD and A have approximately the same impurity levels and the same PSD and standard chemistry. This indicates that the higher BF layer bubble content in crucible STD is a fusion related problem and not due to the sand quality. However, crucible B has the lowest BF layer bubble density, both for the sub-detection limit bubbles and in general. As crucible B has the finest PSD and chemistry, the BF layer bubble content and evolution are also likely to be related to sand quality.

To draw a conclusion, the STD crucible shows the greatest variation in BF layer bubble content when considering the crucibles from both batches. Furthermore, the STD crucible from this work has by far the highest BF layer bubble content of the crucibles under investigation. It is important, however, to understand that this does not have to be a trend for all STD crucibles. Keep in mind that the STD crucible from the Project work had the lowest BF layer bubble content. It is crucible B which experiences, on average, the lowest bubble volume expansion with time and temperature and in general the most promising results in the tests performed in this work. It must be considered that there may be large local variations within a crucible sample. Furthermore, only two crucibles were tested per type, one new and one used. Therefore, the statistic is too low to conclude on any trends.

# 7 Further work

Considering any further work, it would be interesting to observe the bubble growth when the temperature is increased beyond what is normal for a crystal pulling process. This could give more information on the nature of the bubble growth and how it develops with time. It would also be interesting to observe and follow the growth of the same bubble before and after heat treatment. This would be possible with 3D modelling, e.g. in ImageJ. Furthermore, more crucibles should be investigated to test the reproducibility of the results.

# References


[1] M. A. Maehlum: "Which Solar Panel Type is Best? Mono vs. Polycrystalline vs. Thin Film", 2015. Downloaded 13.06.2017 from: energyinformative.org

[2] J. Aleksic, P. Zielke, J. A. Szymczyk et al: "Temperature and Flow Visualization in a Simulation of the Czochralski Process Using Temperature-Sensitive Liquid Crystals", 2002.

[3] Information on quartz sand quality.
Downloaded 06.10.2016 from: thequartzcorp.com/en/products

[4] S. H. Hansen: "Characterization of quartz crucibles for silicon solar cell production" (my own Project Work), 2016.

[5] "Overview of silica polymorphs". Downloaded 04.05.2017 from:
quartzpage.de/gen_mod.html

[6] J. Götze, R. Möckel: "Quartz: Deposits, Mineralogy and Analytics", Springer, 2012.

[7] G. Coletti: "Impurities in silicon and their impact on solar cell performance", 2011.

[8] K. L. Sandvik: "Oppredning av primære og sekundære råstoffer", Tapir, 1999.

[9] G. J. Jameson: "Flotation cell development", 1992.

[10] B. W. Atkinson, C. J. Conway and G. J. Jameson: "High-efficiency flotation of coarse and fine coal," in: High-efficiency Coal Preparation: An International Symposium, 1995.

[11] Picture of a ball mill. Downloaded 01.05.2016 from:
linkedin.com/pulse/ball-mill-highly-efficient-grinding-milling-machine-evita-lee

[12] Picture of flotation process. Downloaded 20.11.2016 from:
global.britannica.com/technology/flotation-ore-dressing

[13] B. H. W. S. De Jong, R. G. C. Beerkens, P. A. van Nijnatten: "Ullmann's encyclopedia of industrial chemistry", Wiley, 2000.

[14] V. Lindroos, M. Tilli, A. Lehto, T. Motooka: Handbook of Silicon Based MEMS Materials and Technologies, chapter 2: "Czochralski growth of silicon crystals", 2009.

[15] Private conversation with Norsun representative Y. Hu and J. Ahn.

[16] US Patent US 4632686 A (1986). Downloaded 01.09.16 from:
www.google.com/patents/US4632686

[17] US Patent US 4416680 A (1983). Downloaded 01.09.16 from:
www.google.com/patents/US4416680

[18] Picture of Czochralski puller. Downloaded 01.05.2017 from:
meroli.web.cern.ch/meroli/images/lecture_silicon_growth/clip_image005.jpg

[19] A. Bandarenka, Lecture 7 in "Energy Materials 2", TUM Department of physics, Spring 2016.

[20] US Patent US 5976247 (1999). Downloaded 04.09.2016 from:
www.google.com/patents/US5976247

[21] T. Minami, S. Maeda, M. Higasa, K. Kashima: "In-situ observation of bubble formation at silicon melt–silica glass interface", 2010.

[22] K. Nakajima, N. Usami: "Crystal Growth of Silicon for Solar Cells", Springer, 2009.

[23] X. Huang, H. Kishi, S. Oishi, H. Watanabe, K. Sanpei, S. Sakai and K. Hoshikawa: "Expansion Behavior of Bubbles in Silica Glass Concerning Czochralski (CZ) Si Growth", 1999.

[24] J. J. Biernacki, G.P Wotzak: "Stoichiometry of the C+$SiO_2$ reaction", 1989.

[25] Picture of quartz structure with OH groups. Downloaded 02.04.2017 from:
www.slideshare.net/fizanchee/types-of-chromatography

[26] F. W. Thorsen: "Investigation on Quartz Crucibles for Monocrystalline Silicon Ingots for Solar Cells", Master Thesis, 2016.

[27] J. C. Elliot, S. D. Dover: "X-ray microtomography", Wiley, 1982.

[28] Tutorial on "X-ray computed tomography". Downloaded 12.11.2016 from: serc.carleton.edu

[29] Tutorial on "Basics of X-ray production". Downloaded 12.11.2016 from:
radiologymasterclass.co.uk

[30] "Microscopes, Lesson 2". Downloaded 28.08.2016 from:
msnucleus.org/membership/html/jh/biological/microscopes/lesson2/microscopes2c.html

[31] G. I. Goldstein, D. E. Newbury, P. Echlin, D. C. Joy, C. Fiori, E. Lifshin: "Scanning electron microscopy and x-ray microanalysis", New York: Plenum Press, 1981.

[32] Picture of optical compound microscope. Downloaded 13.02.2017 from:
ammrf.org.au/myscope/images/sem/sem-ve-lm.png

[33] P. R. Griffiths, J. A. de Haseth: "Fourier Transform Infrared Spectrometry, second edition, 2007.

[34] "How an FTIR Spectrometer Operates".
Downloaded: 25.01.2017 from: chem.libretexts.org

[35] B. Sloots: "Measuring the low OH content in quartz glass", 2008.

[36] T. Hansen: "Cristobalite Inversion". Downloaded 07.09.2016 from:
www.digitalfire.com/4sight/glossary

[37] H. Hendrickx: "Cristobalite formation on quartz crucibles inner surface for CZ solar cell ingot production", Master Thesis, 2017.

[38] C. Brechignac, P. Houdy, M. Lahmani: Nanomaterials and Nanochemistry, chapter 1: "Size effects on structure and morphology of free or supported nanoparticles", Springer, 2007.

[39] G. L. Squires: "Practical Physics, Fourth Edition", Cambridge, 2001.

[40] J. A. Bones: CGSim simulation of Czochralski puller, 2017.

[41] ICP-MS measurements performed on the crucibles under investigation by the Quartz Corp, 2017.

[42] Private conversation with the Quartz Corp representative A. M. F. Muggerud.

# 8 Appendix

## 8.1 ImageJ script - Finding the bubble percent

```
var sliceRange = getString("Slice Range:", "200-1200");
run("Make Substack...", " slices="+sliceRange);
setSlice(nSlices/2);
//setAutoThreshold("Default");
//run("Convert to Mask", "method=Default background=Light calculate list");
//setOption("BlackBackground", false);
setThreshold(0,12000);
run("Convert to Mask", "method=Default background=Light");
run("Divide...", "value=2.55 stack");
run("Measure Stack");
run("Summarize");
selectWindow("Results");
```

## 8.2 MATLAB script - Finding the OH content

```
data = load('RawData.txt');
y = data(2900:5500,2);
(ycorrect, baseline) = bf(y,5,'confirm');
d = 2;
Tmin = min(1-abs(ycorrect));
beta=(1/d)*log(1/Tmin);
factor = (17*10000)/(77.5*2.21);
OHppm=factor*beta;
```